Title

The Role of TCF7L2 in Regulating Energy Metabolism in Thalamocortical Circuitry and its Broader Impact on Social Behavior

Running Title

TCF7L2 in Thalamocortical Energy Metabolism and Behavior

Authors

Andrzej Nagalski[1*], PhD;

Kamil Koziński[1*], PhD;

Suelen Baggio[1*], PhD;

Łukasz M. Szewczyk[1], PhD;

Marcin A. Lipiec[1,2], PhD;

Ben Hur M. Mussulini[1,3], PhD;

Michael O. Gabriel[1], PhD;

Joanna Bem[1], PhD;

Ksenia Meyza[2], PhD;

Anna Goncerzewicz[2], PhD;

Ludwika Kondrakiewicz[2], MS;

Konrad Danielewski[2], MS;

Dariusz Gołowicz[1], PhD;

Anna Kiryk[4], PhD;

Urszula Wojda[4], Professor;

Krzysztof Kazimierczuk[1], Professor;

Ewelina Knapska[2], Professor;

Agnieszka Chacińska[3], Professor;

Marta B. Wiśniewska[1**], Professor

1. Centre of New Technologies, University of Warsaw, Poland

2. BRAINCITY - Centre of Excellence for Neural Plasticity and Brain Disorders, Nencki Institute of Experimental Biology, Warsaw, Poland

3. International Institute of Molecular Mechanisms and Machines (IMol), Warsaw, Poland

4. Center of Neurobiology, Nencki Institute of Experimental Biology, Warsaw, Poland

* equal contribution

**corresponding author: Centre of New Technologies, University of Warsaw, ul. Banacha 2C, 02-097 Warsaw, Poland, (+48)661617010, m.wisniewska@cent.uw.edu.pl

Abstract

Psychiatric and metabolic disorders often co-occur. While shared genetic factors and cellular dysfunctions are implicated, the underlying molecular mechanisms remain poorly understood. TCF7L2, a risk gene for type 2 diabetes and autism spectrum disorder, is highly expressed in the thalamus—a brain region extensively interconnected with the cortex, playing a key role in sensory processing, motor control, and behavioral regulation. Given its known role as a transcription factor regulating systemic energy metabolism, we explored its potential contribution to brain metabolism and behavior. To this end, we used a conditional knockout model with postnatal TCF7L2 loss in the thalamus and partial deficiency in the pancreas. *Tcf7l2* knockout mice exhibited social deficits and reduced motor habituation. In parallel, they also developed systemic glucose intolerance, modelling the psychiatric-metabolic comorbidity. Thalamic depletion of TCF7L2 resulted in elevated inhibitory phosphorylation of the pyruvate dehydrogenase —an enzymatic gatekeeper for pyruvate utilization in energy production—in the thalamus and cortex. This was accompanied by altered thalamic and cortical metabolism, characterized by reduced efficiency of pyruvate oxidation alongside enhanced oxidation of fatty acids and ketone bodies. Notably, a ketogenic diet alleviated metabolic dysregulation in the brain and normalized some social behaviors in knockout mice. These findings suggest that impaired energy metabolism in the thalamocortical circuitry may represent one of the pathogenic mechanisms underlying neuropsychiatric symptoms.

Introduction

The prevalence of metabolic disorders is higher in individuals with psychiatric conditions. This association is particularly evident in autism spectrum disorder (ASD) and schizophrenia (SCZ), where the risk of developing metabolic conditions like type 2 diabetes or dyslipidemia is increased [1–4]. These disorders may influence each other's onset or progression and also appear to share genetic risk factors, dysregulated cell signaling pathways and mitochondrial dysfunctions, suggesting potential common origins [5–8]. However, the molecular mechanisms linking metabolic and psychiatric disorders remain unclear.

Wnt/β-catenin signaling is one of the molecular pathways implicated in metabolic and psychiatric disorders [9–11]. In particular, TCF7L2, a key effector transcription factor in the Wnt pathway, is predominantly expressed in metabolic organs and the brain. Variants of the *TCF7L2* gene are among the strongest genetic risk factors for type 2 diabetes [12–14]. TCF7L2 is essential for peripheral metabolic homeostasis, regulating metabolic organ development [15,16], insulin production and secretion in pancreatic β-cells [17,18], metabolic adaptation in the liver [19,20], and lipid metabolism in adipose tissue [21,22]. Beyond its role in diabetes, genetic variations in this gene have been associated with ASD and SCZ [10,23–26]. Recently, mutations in *TCF7L2* have been identified as the cause of a rare neurodevelopmental disorder presenting with a spectrum of symptoms, including motor delay, intellectual disability, and features of autism, with variable expression across individual [27] (https://trndnetwork.org/trnd/signs-symptoms/).

In the brain, TCF7L2 is highly expressed in neurons within subcortical regions involved in sensory processing and behavioral response, where it promotes the expression of genes involved in connectivity development and maintenance of electrophysiological properties [28–30], oligodendrocyte precursors and young astrocytes [24,31–34]. At the behavioral level, TCF7L2

79 regulates nicotine intake through habenular neurons [35], vocalization via periaqueductal grey
80 neurons [36], and sociability through astrocytic functions [24]. Nevertheless, the role of TCF7L2 in
81 brain function and its contribution to the pathogenesis of ASD and SCZ remains far less
82 understood than its role in metabolic organs.

83 The thalamus maintains the highest levels of TCF7L2 in the brain [29]. This subcortical
84 brain structure and its reciprocal cortical connections play a key role in modulating
85 sensorimotor signaling and participate in various cognitive and behavioral functions [37–40].
86 Neuroimaging studies repeatedly showed aberrant thalamocortical connectivity in ASD and
87 SCZ individuals [41–49], suggesting thalamic dysfunctions in the pathogenesis of those disorders.
88 Similarly, in mice, thalamocortical connection impairments were observed in classical models
89 of ASD [50,51], and activity of specific thalamic nuclei was linked to social deficits [52–58].
90 Furthermore, studies in genetic models confirmed a causal link between certain ASD risk
91 genes, thalamic dysfunctions and ASD-relevant phenotypes, including attention deficits,
92 seizures, sleep fragmentation, increased self-grooming, sensory disturbances and social
93 deficits [59–62], with one study also reporting social deficits [63]. They also highlighted the
94 association between impaired neuronal inhibition linked to channelopathies and these
95 phenotypes. However, experimental confirmation that thalamic dysfunction driven by ASD
96 risk gene loss underlies core ASD manifestations— such as behavioral inflexibility and reduced
97 sociability—remains limited, and other cellular mechanisms have yet to be explored.

98 Here, we demonstrate that postnatally induced deficiency of TCF7L2 in the thalamus
99 affects social performance and motor flexibility in mice. We demonstrate that TCF7L2 plays a
100 role in regulating energy metabolism in both the thalamus and cortex. Furthermore, we
101 provide evidence that metabolic interventions can normalize brain metabolism and partially
102 rescue behavioral deficits caused by *Tcf7l2* knockout, experimentally linking ASD with

103 metabolic dysfunctions in the brain. Therefore, we propose that an imbalance in energy
104 metabolism in the thalamocortical circuit can contribute to ASD pathomechanism.

105 Results

106 *Cck*-driven Cre-mediated recombination of *Tcf7l2* removes TCF7L2 from the thalamus and 107 partially from the pancreas, inducing a concurrent prediabetic state

108 To examine the role of thalamic TCF7L2 in the development of social impairments and
109 metabolic dysfunctions, we generated a conditional knockout of *Tcf7l2* in cells expressing the
110 cholecystokinin (*Cck*) gene, whose expression overlaps with *Tcf7l2* expression in neurons in
111 the thalamus. Crossing *Tcf7l2* floxed ($Tcf7l2^{fl/fl}$) mice with Cck^{Cre} animals results in the loss of
112 TCF7L2 in most thalamic nuclei by postnatal day 14 (P14), as demonstrated in our previous
113 study [31] (Fig. S1A–B, a schematic overview of the affected nuclei), and this loss was confirmed
114 here at P60 (Fig. 1 A-B). We did not observe the knockout in other *Tcf7l2*-expressing brain
115 regions, such as habenulae, dorsal midbrain [31] or hypothalamus (SFig. 2).

116 Given the metabolic focus of this research, it was important to first assess potential
117 TCF7L2 deficiency in the Cck^{Cre}:$Tcf7l2^{fl/fl}$ strain, hereinafter referred to as *Tcf7l2*-cKO, in the
118 pancreas, liver and duodenum, where TCF7L2 plays a well-established role in regulating
119 peripheral metabolism. To this end, we examined whether the *Cck* transgenic promoter drives
120 *Cre* expression in the abovementiones organs using the Cck^{Cre}:$TdTomato^{fl/fl}$ reporter line, and
121 evaluated the impact of the conditional knockout on TCF7L2 expression.

122 We observed a TdTomato signal in numerous pancreatic cells, consistent with the
123 moderate expression of *Cck* in the pancreas [64,65] which also stained positive for TCF7L2 (Fig.
124 1C). Histological features of these cells were characteristic of β-cells, suggesting that TCF7L2
125 could be removed from these cells. Western blot analysis further confirmed this, showing a

126 decrease in TCF7L2 levels in the pancreas from *Tcf7l2*-cKO mice (Fig. 1D), indicating a partial
127 pancreatic deficiency of TCF7L2 in our model.

128 In the liver, sparse TdTomato-positive cells were TCF7L2-negative (Fig. 1E). Their
129 morphology and localization in the lumen of blood vessels indicated that they were not
130 hepatocytes but either epithelial or Kupffer cells. This suggested a hepatocyte-specific gene
131 knockout was unlikely. Unexpectedly, the level of TCF7L2, assessed by Western blot,
132 increased in the liver (Fig. 1F), possibly as a secondary effect of the pancreatic knockout.

133 In the duodenum, TCF7L2-positive cells localized in crypts, while sparse TdTomato-
134 positive cells were TCF7L2-negative (SFig. 3), excluding *Tcf7l2* knockout in this organ. The
135 localization of TdTomato-positive cells was consistent with the localization of *Cck*-expressing
136 enteroendocrine cells [66].

137 Decreased TCF7L2 levels in the pancreas and increased levels in the liver suggested a
138 complex misregulation of *Tcf7l2* expression in our model, potentially contributing to
139 metabolic dysfunction. To test this, we assessed body weight, glucose, and insulin levels in
140 control and *Tcf7l2*-cKO mice fed either a standard chow (66% energy from carbohydrates) or
141 high-fat (HF, 60% energy from fat) diets for six weeks (Fig. 1G). On the chow diet, control and
142 *Tcf7l2*-cKO mice gained weight similarly (Fig. 1H). Fasting insulin and glucose levels were also
143 comparable (Fig. 1I-J), but *Tcf7l2*-cKO mice showed impaired glucose clearance (Fig. 1K).
144 Under the HF diet, metabolic differences became more pronounced: *Tcf7l2*-cKO mice gained
145 significantly more weight (Fig. 1H), exhibited elevated fasting insulin and glucose (Fig. 1I-J),
146 and showed exacerbated glucose intolerance (Fig. 1K).

147 Our approach effectively eliminated TCF7L2 from most thalamic neurons and partially
148 from pancreatic β-cells. Consequently, the transgenic mice displayed a prediabetic state

149 alongside potential thalamic impairments, rendering them suitable for investigating the
150 comorbidity of thalamus-related psychiatric disorders and metabolic dysfunctions.

151 *Cck*^{Cre}:*Tcf7l2*$^{fl/fl}$ mice show no evidence of impairment in basic locomotor parameters, anxiety-
152 like behavior, or major cognitive deficits

153 Patients with mutations in the *TCF7L2* gene exhibit impaired motor function,
154 increased anxiety, cognitive disabilities and difficulties with social interaction [27]. To determine
155 if postnatal thalamic ablation of TCF7L2 could lead to similar behaviors, we conducted a series
156 of behavioral tests in *Tcf7l2*-cKO mice. Both adult males and females were included unless
157 otherwise noted.

158 We started with assessing basic locomotor and sensorimotor performance.
159 Locomotor functions were evaluated in a dimly lit, non-anxiogenic enclosure enriched with
160 objects (Fig. 2A). Under these conditions, CTR and *Tcf7l2*-cKO mice displayed comparable
161 immobility times, average and maximal speeds, and angular velocity, in both sexes (Fig. 2B-
162 D). We then assessed olfactory function using a buried food-seeking test (Fig. 2E). Latency to
163 retrieve the food did not differ between genotypes (Fig. 2F). These results showed intact
164 locomotor and sensorimotor functions *Tcf7l2*-cKO mice under low-demand conditions.

165 Next, to assess risk-taking and anxiety-related behaviors, we used the light–dark box
166 (SFig. 4A) and open-field (Fig. 2G) apparatuses. In the light–dark box, there were no genotype
167 differences in the time spent in the light zone, latency to enter the dark zone, or the number
168 of transitions between compartments (SFig. 4B–D). Similarly, no significant differences were
169 observed between control and *Tcf7l2*-cKO mice in the time spent in the center of the open
170 field (Fig. 2H). Analysis of locomotor activity, however, during the open-field test revealed a
171 genotype-dependent difference. While mice of both genotypes moved at similar speeds along

172 the perimeter (Fig. 2I), control mice increased their locomotor activity in the center, moving
173 faster than at the periphery, with this effect reaching statistical significance in females. In
174 contrast, *Tcf7l2*-cKO mice lacked this modulation, suggesting impaired context-dependent
175 locomotor adjustment. These results indicated that postnatal *Tcf7l2* knockout in thalamic
176 neurons does not induce anxiety-like behaviors but may alter locomotor adaptability.

177 We then assessed cognitive performance using an automated *IntelliCage* system,
178 which tracked individual mice as they visited water bottles in corners within a group-housed
179 setting via implanted transponders (Fig. 2J). Due to aggressive behaviors between males
180 within a group, we tested cohorts composed only of females. The testing protocol consisted
181 of place learning and reward-based discrimination learning tasks, preceded by adaptation
182 phases. During the place learning phase, each mouse learned to access ts individually assigned
183 corner, a task that required spatial associative learning. Females of both genotypes
184 performed equally well, as measured by an increasing percentage of correct visits (Fig. 2K).
185 During the reward-based learning phase, one of the two bottles in the assigned corner was
186 filled with sweetened water. Mice from both groups rapidly developed a preference for the
187 rewarding bottle (Fig. 2L), with no significant differences in performance. These results
188 suggested no overt deficits in spatial or reward-based learning and motivation in *Tcf7l2*-cKO
189 mice under these conditions.

190 Postnatal thalamic knockout of *Tcf7l2* leads to social deficits and reduced motor habituation

191 In the next part of the behavioral testing, we focused on social behaviors, using the
192 classic three-chamber test (interest in social stimulus), the *IntelliCage* system (group
193 preference for a corner during the simple adaptation phase), and the *EcoHAB* setup (dynamic
194 and passive interactions within a group).

195 We began with evaluating the mice's interest in social over non-social interactions in
196 the three-chamber test (A). In the apparatus, mice were exposed to an unfamiliar mouse
197 under one cup (social stimulus) and a new inanimate object (non-social stimulus) under
198 another. Control mice spent significantly more time interacting with the mouse than with the
199 object (Fig. 3B). Similarly, *Tcf7l2*-cKO males displayed normal social interest. In contrast,
200 knockout females exhibited a marked impairment in social preference, as evidenced by a
201 significantly lower discrimination index.

202 Next, we used the *IntelliCage* system, in which water bottles were located in four
203 corners, over a three-day adaptation period (Fig. 3C) to examine whether patterns of corners'
204 visitations reflect social coordination and differ between genotypes. Females of both
205 genotypes visited the *IntelliCage* corners at overall similar levels throughout the adaptation
206 phase (Fig. 3D). Control females showed a reduction in corner visitation already on day 2,
207 whereas a similar decrease in *Tcf7l2*-cKO females was observed on day 3. This temporal shift
208 may indicate a delay in locomotor habituation in knockout mice.

209 Despite decreased visitation levels, control females exhibited a statistically significant
210 emergence of a shared corner preference. By day 3, nearly 40% of all visits were directed
211 toward a single common corner (Fig. 3E and SFig. 5A-B). Unlike control animals, *Tcf7l2*-cKO
212 females failed to form such a group-level bias, suggesting decreased sensitivity to social cues.

213 Subsequently, to further investigate how female *Tcf7l2*-cKO mice interact within a
214 group, we employed the *EcoHAB* system, which has been previously used to test mouse
215 models of autism [67]. In this naturalistic setup, female lived together for several days in a four-
216 cage setup connected by tunnels (Fig. 3F). Each mouse was individually identified with an
217 implanted transponder, and its movements between cages were continuously tracked.

We first analyzed exploratory behavior by counting the number of visits to all cages in three consecutive days (dark phases). On day 1, *Tcf7l2*-cKO mice made significantly fewer passages than control mice (Fig. 3G). In both groups, exploration declined on days 2 and 3; however, the reduction was smaller in *Tcf7l2*-cKO mice, with a decrease of approximately 25% in controls and 15% in *Tcf7l2*-cKO mice (SFig. 5C-D), suggesting reduced motor habituation, similar to *Intellicage*.

To assess dynamic social interactions during this period, we counted the number of times one mouse chased another during passages between cages through the connecting tunnels, for each pair. Control mice showed high in-pair chasing on average on the first day, with about a 40% decline in the subsequent days (Fig. 3H, violin plot; SFig. 5E, bar plot). This pattern was expected, as typical social behavior involves an initial increase in interactions to establish a social structure, followed by a decrease as the hierarchy forms. In contrast, *Tcf7l2*-cKO mice exhibited significantly reduced in-pair chasing levels. The effect was particularly pronounced on day 1, when in-pair-chasings were nearly twofold less frequent compared to control cohort.

Moreover, heatmaps of chasing interactions and their directionality (Fig. 3I) revealed individually specific patterns of social engagement: some mice were predominantly chasing, others were mostly being chased, some exhibited a similar level of chasing and being chased, and others showed minimal involvement in either behavior. Variability in in-pair chasing behavior was more pronounced in control mice, a difference between genotypes that was statistically confirmed by Levene's test ($p < 10^{-8}$, $p < 0.001$, and $p = 0.02$ for control–*Tcf7l2*-cKO comparisons on days 1, 2, and 3, respectively). Pearson's correlation analyses across consecutive days revealed that individual chasing patterns were stable across consecutive

241 days (SFig. 5F), indicating that the observed variation reflected consistent behavioral
242 tendencies rather than random fluctuations. Notably, this temporal stability between day 1
243 and 2 was greater in control mice than in *Tcf7l2*-cKO mice. Together, these findings indicated
244 that genotype-dependent differences in chasing affected not only the overall level, but also
245 the structure of social engagement.

246 Our previous work showed that chasing behavior serves to manifest dominance [68],
247 and the results described above further indicated that chasing captures stable, individual-
248 specific patterns of social organization within the group. Nevertheless, to rule out the
249 possibility that reduced chasing in *Tcf7l2*-cKO mice is a consequence of lower exploratory
250 drive, we normalized the data by calculating the proportion of socially motivated passages
251 (i.e., chasing) relative to the total exploratory activity of a mouse (SFig. 5G). This proportion
252 was significantly lower in *Tcf7l2*-cKO mice, supporting reduced active social engagement. In
253 addition, Pearson's correlation analysis revealed that exploration correlated weakly or not at
254 all with being chased, with no statistical significance in most cases (SFig. 6A-G) and moderately
255 with chasing (SFig. 6H-M), indicating that these two components of social behavior relate
256 differently to exploration.

257 As an additional measure of social behavior, we calculated, for each mouse pair, the
258 proportion of their total time spent together that occurred in the cage most preferred by the
259 group (i.e., the cage in which mouse pairs spent the most of their time together on average).
260 All cohorts exhibited some degree of consensus in cage preference, with *Tcf7l2*-cKO mice
261 showing an extreme pattern—spending nearly all of their in-pair time together in a single cage
262 (Fig. 3J-K). These patterns suggested reduced flexibility in how *Tcf7l2*-cKO mice interact with
263 their social environment.

264 Due to aggressive behavior, males were not tested in *EcoHAB*, as was the case in
265 *IntelliCage*. Instead, groups of four unfamiliar males were placed together in a shared cage
266 for two hours (Fig. 3L), during which spontaneous direct social interactions were recorded,
267 including investigative behaviors such as nose-to-nose and anogenital sniffing. During the first
268 30 minutes, *Tcf7l2*-cKO mice exhibited a similar number of nose-to-nose contacts but fewer
269 occurrences of anogenital sniffing compared to controls (Fig. 3M), indicating reduced social
270 investigative behaviors. Notably, while control mice showed a significant reduction in
271 interactions during the subsequent 30-minute intervals (by 30-40%), *Tcf7l2*-cKO mice
272 maintained a steady level of interactions throughout the entire test period, suggesting a lack
273 of short-term social habituation.

274 Taken together, the results from *IntelliCage*, *EcoHAB*, the three-chamber test and the
275 investigative interaction test suggested that *Tcf7l2*-cKO mice have a reduced capacity to adapt
276 their behavior to changing social and environmental conditions.

277 TCF7L2 regulates metabolic genes and metabolic pathways in the thalamus

278 Given TCF7L2's established role in regulating metabolic gene expression in the
279 pancreas [69] and liver [20], we hypothesized that TCF7L2 similarly influences metabolic gene
280 expression in the thalamus. To test this, we analyzed our previous RNA-seq data, focusing on
281 metabolism-associated genes, and integrated the results with our TCF7L2 ChIP-seq data from
282 the same region [31], thalamic expression enrichment from the Allen Brain Atlas (available from
283 mouse.brain-map.org) [70] and cell-type enrichment based on published single-cell RNA-seq
284 data from the thalamus [71].

285 We identified 49 metabolism-related differentially expressed genes (DEGs) in the
286 thalamus of knockout mice compared with control mice, of which 30 were downregulated

287 and 19 were upregulated (Fig. 4A). More than 30% of these genes were characterized by the
288 presence of TCF7L2 ChIP-seq peaks, indicating direct regulation by this factor. The majority
289 were neuron-enriched. Based on their cellular functions, we grouped the genes into
290 categories related to energy metabolism. Within these categories, we identified two
291 particularly interesting gene sets.

292 The first group comprised DEGs involved in PPAR/fatty acids signaling pathways,
293 including nuclear receptor transcription factors *Ppard, Rora*, and *Ppargc1a*, as well as lipid
294 metabolism-related genes *Plin3*, *Plin4*, *Acsl4*, *Acadl*, *Igfbp3,* and *Igfbp5*. The presence of direct
295 TCF7L2 binding sites at *Ppard* and *Rora*—but not at the other genes—suggests that TCF7L2
296 may regulate lipid metabolism indirectly through these nuclear receptors.

297 The second set of DEGs was associated with the protein kinase C (PKC) pathway,
298 known for regulating energy metabolism and glucose homeostasis [72]. (Fig. 4B). This group
299 included phospholipases *Plcb4*, *Plch2* and *Plcd*, a diacylglycerol kinase *Dgkh*, protein kinases
300 *Prkcb*, *Prkcd* (PKCδ), *Prkce*, *Prkch* and *Prkc,* and pyruvate dehydrogenase *Pdk3*. TCF7L2-ChIP-
301 seq peaks were mapped to *Plcb4*, *Prkcb*, *Prkcd* and *Prkch*, suggesting direct regulation of these
302 genes by TCF7L2.

303 We hypothesize that the PDHc/pyruvate pathway might be disrupted in the thalamus
304 in the*Tcf7l2*-cKO mice. This was based on *vitro* evidence that PKCδ can signal to the pyruvate
305 dehydrogenase complex (PDHc) which controls pyruvate utilization in the tricarboxylic acid
306 cycle (TCA) [73], and on data showing elevated serum pyruvate in PKCδ-deficient mice [74]. To
307 investigate our prediction, we compared PKCδ levels and PDHE1α phosphorylation between
308 control and knockout mice using Western blot. As expected from its transcript level, PKCδ was
309 significantly downregulated in the thalamus of *Tcf7l2*-cKO mice (Fig. 4C). Consistent with the

310 predicted signaling pathway, PDHE1α phosphorylation increased, while the total level of
311 PDHE1α remained unchanged.

312 In summary, our findings indicate that TCF7L2 regulates the activity of at least two
313 critical metabolic groups of pathways: the PPARD pathways, through direct control of *Ppard*
314 gene expression, and the PKC/PDHc pathways by directly modulating the expression of genes
315 encoding PKCδ and other proteins associated with the pathway. This regulatory role
316 suggested that TCF7L2 may shape the energy metabolism profile in the thalamus.

317 Deficiency of TCF7L2 alters the profile of energy metabolism in the thalamus and cortex

318 To examine whether the thalamic loss of TCF7L2 affects brain metabolism at the
319 functional level, we began by measuring soluble metabolites associated with glycolysis and
320 the TCA cycle using ^{1}H-NMR spectroscopy. This approach provided a broad overview of over
321 a dozen water-soluble metabolites, most of which were linked to the TCA cycle (SFig. 7A). We
322 analyzed both thalamic and cortical samples, assuming that metabolic impairments in the
323 thalamus might impact the cortex due to the high presence of thalamus-derived presynaptic
324 proteins and mitochondria there. Samples were collected from mice maintained on either the
325 standard chow or HF diet, the latter included to expose potential metabolic defects under
326 metabolic stress (Fig. 4D).

327 In knockout mice on the chow diet, levels of the measured metabolites were
328 comparable to those in controls (Fig. 4E-F and SFig. 7A-D). However, when fed the HF diet,
329 *Tcf7l2*-cKO mice exhibited significantly elevated lactate and alanine—both pyruvate-related
330 metabolites—in the thalamus (Fig. 4E), and increased alanine in the cortex (Fig. 4F). These
331 elevated levels may reflect altered pyruvate utilization, prompting us to further explore brain
332 mitochondrial energy metabolism in these mice.

333 To directly assess mitochondrial oxidative capacity, we performed high-resolution
334 respirometry on isolated thalamic and cortical cells (Fig. 4G), enabling us to evaluate intrinsic
335 mitochondrial function independent of potential in vivo compensatory mechanisms. This
336 analysis was conducted in both sexes.

337 Within mitochondria, pyruvate, ketone bodies and fatty acids are converted to acetyl
338 CoA via distinct pathways: oxidative decarboxylation in the PDHc, oxidation by β-
339 hydroxybutyrate dehydrogenase, and β-oxidation, respectively [75]. To assess the efficiency of
340 these pathways, we supplied our samples with palmitoylcarnitine in the presence of malate
341 and non-limiting levels of ADP, octanoylcarnitine, 3-β-hydroxybutyrate, followed by pyruvate
342 and glutamate. In the mitochondria from *Tcf7l2*-cKO mice, pyruvate oxidation was markedly
343 reduced both in the thalamus and cortex of females and males (Fig. 4H-I). These results were
344 consistent with reduced PDHc activity. In contrast, the oxidation of 3-β-hydroxybutyrate and
345 fatty acid β-oxidation were significantly elevated in the same samples.

346 To determine whether these metabolic alterations were brain region-specific, we
347 measured substrate oxidation rates in cerebellar mitochondria. We chose the cerebellum
348 because it lacks input from the thalamus. No differences were detected in the efficiency of
349 pyruvate oxidation, 3-β-hydroxybutyrate oxidation, or β-oxidation between knockout and
350 control mice (SFig. 8). This finding suggests that the metabolic impairments observed in the
351 cortex and thalamus of *Tcf7l2*-cKO mice were brain-region-specific and were unlikely to be
352 secondary effects of peripheral metabolic changes.

353 Altogether, these findings demonstrate that the deficiency of thalamic TCF7L2 alters
354 the energy metabolism profile in the thalamocortical circuitry, affecting the rates of energy
355 production from different sources.

356 A ketogenic diet mitigates brain metabolic and social deficits induced by thalamic *Tcf7l2*
357 knockout

358 Given the altered brain metabolism and reduced social preference observed in *Tcf7l2*-
359 cKO, we sought to investigate if a ketogenic diet, which has shown promise in treating
360 individuals with ASD [76–78] and is recognized for its potential to modify metabolic pathways [79],
361 could improve their social performance. To test this, we administered a ketogenic diet (94%
362 of energy from fat) for six weeks (Fig. 5A) and assessed its impact on systemic metabolism,
363 brain metabolism and social performance.

364 The ketogenic diet halted weight gain in control mice but did not affect weight gain in
365 *Tcf7l2*-cKO mice compared to the chow diet (SFig. 9A-B). It elevated fasting insulin levels only
366 in *Tcf7l2*-cKO mice (SFig. 9C). Although fasting glucose levels remained unaffected (SFig. 9D),
367 glucose tolerance decreased in both genotypes compared to the chow diet, with a more
368 pronounced effect observed in knockout mice (SFig. 9E). These changes indicated the
369 emergence of insulin resistance, comparable to metabolic effects observed with HF diet
370 exposure. Collectively, these results indicated the ketogenic diet adversely affected systemic
371 metabolism homeostasis in both genotypes.

372 Next, we examined the impact of the ketogenic diet on energy metabolism in the
373 thalamus and cortex using high resolution respirometry (Fig. 5B). Notably, the ketogenic diet
374 normalized respiration rates in both brain regions in *Tcf7l2*-cKO mice, in both females and
375 males (Fig. 5C-D). In particular, pyruvate oxidation levels in knockout mice increased to levels
376 comparabe to those of control animals. Thus, surprisingly, while systemic metabolism
377 deteriorated, the ketogenic diet led to improvements in brain energy metabolism.

Finally, we assessed the effects of ketogenic diet on social behavior and locomotor habituation using the three-chamber test and the *EcoHAB* system (in females), as well as a spontaneous social direct interaction test in a group of unfamiliar mice (in males).

In the three-chamber test (Fig. 5E), the ketogenic diet did not affect social preference in control females but increased interest in the unfamiliar mouse in *Tcf7l2*-KO females, restoring their preference to control levels (Fig. 5F).

In *EcoHAB* (Fig. 5G), the ketogenic diet reduced exploratory behavior in control mice while increasing it in *Tcf7l2*-cKO mice (Fig. 5H), thereby eliminating the genotype-related difference observed under standard diet conditions (Fig. 5H; compare with Fig. 3G). Simultaneously, the ketogenic diet restored locomotor habituation in *Tcf7l2*-cKO mice (SFig. 10A-C; compare with SFig. 5D), as indicated by an approximately 50% reduction in cage visits—an even greater decrease than that observed in controls (30%). Similarly, in-pair chasing interactions declined in control mice on day 1, reaching levels observed in *Tcf7l2*-cKO mice, and with both genotypes showing a marked day-to-day reduction in chasing events, indicative of social habituation (Fig. 5I, violin plot; Fig. 5J, heatmap; SFig. 10D, bar plot; compare with Fig. 3H-I and SFig. 5E). The diet, however, had no effect on grouping preferences: while control mice exhibited more flexible spatial use during social interactions, *Tcf7l2*-cKO mice retained rigid preferences for specific social grouping within defined locations (Fig. 5K-L).

In a group of unfamiliar males (Fig. 5M), the ketogenic diet reduced the number of spontaneous social investigative interactions by approximately 30-40% (Fig. 5N; compare with Fig. 3M), resembling the reduction in social exploration observed in females tested in the *EcoHAB* system. The short-time-dependent decline in investigative interactions observed

401 under the standard diet was abolished after ketogenic diet treatment, with both *Tcf7l2*-cKO
402 and control males maintaining a relatively stable number of interactions across time bins.

403 In conclusion, the ketogenic diet effectively normalized energy metabolism in the
404 thalamocortical circuitry of TCF7L2-deficient mice. While it influenced behavior in control
405 animals, it also alleviated certain behavioral deficits in *Tcf7l2*-cKO mice, supporting a possible
406 link between brain metabolic dysfunctions and impairments in social behavior and locomotor
407 patterns.

408 **Discussion**

409 We uncovered that TCF7L2 contributes to social behavior and locomotor flexibility via
410 its thalamic functions. We also demonstrated that TCF7L2 regulates energy metabolism in the
411 thalamocortical circuit by modulating metabolic gene expression in the thalamus.
412 Furthermore, we showed that dietary intervention can alleviate both brain metabolic
413 impairments and some behavioral alterations caused by TCF7L2 deficiency.

414 *Shared risk gene mutations as a cause of comorbidity between metabolic and psychiatric*
415 *disorders*

416 Our results highlight that the frequent comorbidity between systemic metabolic and
417 psychiatric disorders may stem from mutations in shared risk genes, with *TCF7L2* representing
418 one such factor. Misregulation of *Tcf7l2* in metabolic organs leads to glucose intolerance and
419 insulin resistance, while disrupting *Tcf7l2* in postnatal thalamic neurons alters energy
420 metabolism in the thalamocortical circuitry and leads to social deficits. Notably, this
421 conclusion is consistent with a recent human study that identified TCF7L2 as a key regulator
422 in protein networks dysregulated in metabolic and mental disorders [80].

423 While numerous models exist for either metabolic impairments or mental disorders,
424 integrated models that reflect the co-occurrence of both conditions are rare. Our *Tcf7l2*
425 knockout model combines postnatal impairments in the thalamocortical system with poor
426 glucose control in the periphery likely due to a partial knockout in the pancreas alongside an
427 increase in TCF7L2 levels in the liver. This model aligns with existing models of TCF7L2-
428 associated metabolic impairments in the periphery because high fasting plasma glucose levels
429 or glucose intolerance have been observed in mice with either pancreatic knockout of *Tcf7l2*
430 or *Tcf7l2* overexpression in the liver [19,81–84]. Consequently, our study offers a useful model for
431 exploring the interaction between systemic metabolic disorders and mental disorders
432 associated with thalamocortical dysfunction.

433 *Thalamocortical impairment as a cause of autism spectrum disorder*

434 Symptoms frequently accompanying ASD—sensory processing abnormalities,
435 impaired attention, seizures, and disrupted sleep—have been observed in mouse models
436 carrying mutations in ASD risk genes (*Shank3*, *Tsc1*, *Ptchd1*, and *Cntnap2*), in which thalamic
437 dysfunction has been implicated [59–62]. A recent study focusing on the thalamic reticular
438 nucleus, an inhibitory structure that regulates the activity of the proper thalamus, reported
439 social deficits [63]. These findings indicate that thalamocortical dysfunction may primarily
440 contribute to ASD-related phenotypes. Our results extend this framework by demonstrating
441 that reduced social interest—a core ASD-related feature—as well as locomotor inflexibility
442 can also originate from thalamic circuit disruptions, even when these occur postnatally, as in
443 our model. This highlighting the broader role of the thalamus and its developmental trajectory
444 in ASD pathophysiology.

445 Our findings revealed a complex pattern of behavioral alterations in *Tcf7l2*-cKO mice.
446 On one hand, these animals exhibited diminished interest in social stimulus, reduced social
447 chasing behavior (a key component of hierarchy formation [68]), rigid social grouping
448 preferences and a failure to respond to social cues. Collectively, these deficits point to
449 impaired group-level social dynamics. On the other hand, *Tcf7l2*-cKO mice showed decreased
450 general exploration and impairments in locomotor habituation and adaptation. These
451 observations suggest that postnatal loss of TCF7L2 in the thalamus leads to reduced
452 behavioral flexibility in response to changing environment and social contexts.

453 These findings raise the question of which specific thalamic nuclei may underlie the
454 observed behavioral deficits. Identifying the specific thalamic nuclei responsible for social
455 behaviors remains challenging. Higher-order nuclei may be involved, such as those that
456 interact with the prefrontal cortex or nonspecific nuclei project to multiple brain regions.
457 Indeed, the nucleus reuniens, posterior intralaminar complex and the mediodorsal nucleus
458 have been linked to social behaviors in mice [52–58]. Notably, the reduced engagement in
459 chasing behavior in our model may point to involvement of the mediodorsal thalamus, as
460 activity within the mediodorsal thalamus–prefrontal cortex circuit has been shown to play a
461 critical role in regulating social dominance [52,53]. Another possibility is that these deficits result
462 from generalized sensory filtering issues within the thalamus. Sensory dysregulation is known
463 to emerge early in the progression of ASD and is strongly implicated in social functioning
464 deficits [85,86]. Further studies are needed to clarify which thalamic regions contribute to
465 TCF7L2-related social impairments and to uncover the underlying mechanisms.

466 *Linking energy metabolism to the etiology of mental disorders*

467 Our findings adds to the growing body of evidence that dysregulated energy
468 metabolism in the brain plays a crucial role in the etiology of mental disorders [87,88]. In
469 particular, our data point to a relationship between altered glucose metabolism within
470 thalamocortical circuits and ASD-relevant behavioral phenotypes, although a causal link
471 remains to be established. This aligns with clinical studies showing elevated levels of glycolysis
472 products—pyruvate, alanine, and lactate—in the blood of individuals with ASD, as well as
473 elevated cerebral lactate levels [89–94], suggesting enhanced aerobic glycolysis. Similarly, our
474 model exhibited elevated lactate and alanine levels alongside reduced pyruvate oxidation in
475 the thalamus and cortex. This indicates a shift in energy metabolism from glucose oxidation
476 toward alternative energy substrates such as fatty acids and ketone bodies. The *Tcf7l2*-cKO
477 knockout model thus provides experimental support for the Warburg effect hypothesis in ASD
478 [94] and establishes these mice as a relevant model for studying metabolic dysfunctions in ASD
479 and other mental disorders.

480 At the molecular level, these metabolic alterations observed in the thalamocortical
481 circuit in our mouse model may reflect dysregulation of gene networks involved in lipid and
482 glucose metabolism. In particular, thalamic TCF7L2 deficiency altered the expression of genes
483 involved in lipid metabolism, including the key transcriptional regulators PPARD and RORA, as
484 well as glucose metabolism regulators such as PKCδ; the latter two are enriched in the
485 thalamus (see mouse.brain-map.org). The PKCδ is a likely regulator of the pyruvate
486 dehydrogenase complex [73,74], which catalyzes the critical step for pyruvate entry into the TCA
487 cycle. In *Tcf7l2* knockout mice, we observed reduced levels of PKCδ alongside increased
488 phosphorylation of PDHEα, providing preliminary evidence for the disruption of the
489 hypothetical TCF7L2-PKCδ-PDHc regulatory axis.

490 Strikingly, this metabolic disruption affected the thalamus and the cortex, even though
491 the knockout was restricted to the thalamus. This may be attributed to the extensive synaptic
492 connections between thalamic neurons and cortical regions. Another possibility is that brain
493 effects are a consequence of changes in systemic metabolism. However, two observations
494 argue against this possibility. First, the cerebellum, which lacks direct thalamic input, showed
495 no metabolic abnormalities, pointing to the specificity of changes in the thalamocortical
496 circuit. Second, while the ketogenic diet normalized metabolite oxidation in the thalamus and
497 cortex, it did not improve peripheral glucose homeostasis, suggesting that the observed brain
498 effects were not driven by systemic metabolic alterations.

499 These circuit-level metabolic alterations may have direct clinical relevance. Reduced
500 activity of the PDH complex in the thalamocortical circuit may represent a convergent point
501 in the etiology of a subset of individuals with ASD and SCZ, given that the gene encoding the
502 key PDHE1α (PDHA1) subunit of the PDHc is an ASD-risk gene, and autoantibodies against this
503 protein—potentially disrupting PDHc activity—are found in some patients with SCZ [95]. This
504 disruption in glucose metabolism offers a potential target for therapy, as the ketogenic diet,
505 already used in individuals with congenital pyruvate dehydrogenase deficiency [96,97], has
506 shown effectiveness in *Tcf7l2*-cKO mice, supporting its therapeutic potential for a specific
507 group of patients. However, it is important to recognize that, despite its expected benefits for
508 brain metabolism demonstrated in the present study, long-term use of the ketogenic diet
509 might have side effects in both mouse models [98,99] and humans [100] .

510 In our model, we observed a co-occurrence of metabolic impairments in the brain and
511 behavioral abnormalities. However, electrophysiological disturbances have also been
512 identified in the same model [31], and other alterations may be present as well. Thus, it remains
513 unclear whether the metabolic deficits are causally related to the observed behavioral

514 phenotypes. The fact that the ketogenic diet led to improved brain metabolism and behavior
515 provides a potential clue, although the nature of this relationship remains to be established.
516 Investigating the relationship between *Tcf7l2*-related metabolic alterations in the brain and
517 behavioral deficits will be the focus of future studies.

518 *Conclusion*

519 In conclusion, our findings highlight a potential link between disrupted energy
520 metabolism in the thalamocortical circuitry and the etiology of mental disorders such as ASD
521 and SCZ, while emphasizing the role of TCF7L2 in these processes and expanding its known
522 role beyond regulating peripheral metabolism. The observed metabolic shift in energy
523 substrate utilization, with reduced pyruvate oxidation due to thalamic TCF7L2 deficiency,
524 suggests that metabolic dysregulation may directly contribute to neuropsychiatric symptoms.
525 Furthermore, our findings demonstrate that a ketogenic diet can restore both metabolic and
526 social deficits in *Tcf7l2* knockout mice, providing preliminary evidence that dietary
527 interventions may help mitigate the metabolic contributions to mental disorders.

528 **Materials and Methods**

529 *Animals*

530 Thalamus-specific *Tcf7l2* conditional knockout (cKO) mice (Cck^{Cre}:$Tcf7l2^{fl/fl}$) were
531 generated as previously described [31]. Briefly, the C57BL/6NTac-$Tcf7l2^{tm1a(EUCOMM)Wtsi}$
532 ($Tcf7l2^{tm1a}$) mouse strain, which contained with a trap cassette upstream of the critical exon
533 6 of the *Tcf7l2* gene, was first crossed with flippase-expressing mice
534 (Gt(ROSA)26$Sor^{tm1(FLP1)Dym}$; Jackson Laboratory, #009086), and then with mice which
535 expressing Cre recombinase under the control of the *Cck* promoter ($Cck^{tm1.1(cre)Zjh/J}$; Jackson
536 Laboratory, #012706). $Cck^{Cre:}Tcf7l2^{+/+}$ animals were used as controls. To generate the

537 *Cck^{Cre}:TdTomato$^{fl/+}$* reporter strain, *Cck^{Cre}:Tcf7l2$^{+/+}$* mice were crossed with the Ai9(RCL-tdT)
538 strain (Gt(ROSA)26Sor$^{tm9(CAG\text{-}tdTomato)Hze/J}$ Jackson Laboratory, #007909). All animals were
539 housed under standard laboratory conditions (21 ± 2 °C, 60% ± 10% humidity, and 12 h/12 h
540 light/dark cycle), with food and water provided *ad libitum*. Mice aged P60–P90 were used for
541 the tests, unless stated otherwise. All experimental procedures complied with the normative
542 standards of the European Community (Directive 86/609/EEC) and the Polish Government
543 (Dz.U. 2015 poz. 266). Protocols were approved by the Local Ethical Committee No. 1 in
544 Warsaw, and the institutional animal welfare advisory board oversaw animal use at the
545 Centre of New Technologies.

546 *Western blot analysis*

547 Organs and selected brain structures (n = 4 per group) were dissected and
548 homogenized in ice-cold RIPA buffer (50 mM Tris, pH 7.5, Bioshop Life Science Products,
549 #TRS001.1; 50 mM NaCl, Chempur, #794121116; 1% NP-40, Thermo Scientific, #85124; 0.5%
550 sodium deoxycholate, Merck Life Science, #D6750; 0.1% sodium dodecyl sulfate [SDS],
551 Bioshop Life Science Products, #SDS999.500; 1 mM ethylenediaminetetraacetic acid [EDTA],
552 VWR, #E177; 1 mM NaF, Merck Life Science, #67414-1ML-F; EDTA-free protease inhibitor
553 cocktail cOmplete, Roche, #4693132001; phosphatase inhibitor PhosSTOP™, Roche,
554 #4906845001). Protein concentrations were measured using the Protein Assay Dye Reagent
555 (Bio-Rad Laboratories, #5000006). Clarified protein homogenates were separated on SDS-
556 polyacrylamide gels (Bio-Rad, #1610183) and transferred to nitrocellulose membranes (Bio-
557 Rad, #1620112). Membranes were blocked with 10% nonfat dry milk in phosphate-buffered
558 saline (PBS) containing 0.1% Tween 20 (PBS-T) (VWR, #663684B), and incubated overnight at
559 4 °C with the following primary antibodies: anti-TCF7L2 (Cell Signaling Technology, #2569,
560 1:1000), anti-GAPDH (Santa Cruz Biotechnology, #sc-25778, 1:500), anti-PKCδ (Thermo Fisher

561 Scientific, #PA5-17552, 1:1000), anti-PDHE1α (Santa Cruz Biotechnology, #sc-377092,
562 1:30000), anti-phospho-Ser232-PDHE1α (Merck KGaA, #AP1063, 1:500). After washing,
563 membranes were incubated for 2 h at room temperature with secondary antibodies: anti-
564 rabbit IgG peroxidase (Sigma Aldrich, #A0545, 1:10000) or anti-mouse IgG peroxidase (Sigma
565 Aldrich, #A9044, 1:10000). Signal detection was performed using chemiluminescence, and
566 images were captured with an ImageQuant LAS 4000 (Cytiva). Densitometric analyses were
567 conducted using Quantity One 1-D software (Bio-Rad).

568 *Tissue fixation*

569 Mice were anesthetized with a mixture of ketamine (Biowet, 125 mg/kg body weight)
570 and xylazine (Biowet, 10 mg/kg body weight). They were then transcardially perfused with 0.1
571 M PBS, followed by 4.5% paraformaldehyde (PFA; Merck Life Science, #P6148) in PBS. The
572 brain, liver, duodenum, and pancreas were dissected, incubated overnight in 4.5% PFA, and
573 saturated in 30% sucrose (Merck Life Science, #1076515000) in PBS at 4 °C for 24 h. The tissues
574 were subsequently transferred into O.C.T. compound (Sakura Tissue-Tek, #4583) and frozen
575 in -30 °C isopentane (VWR, #24872.298). Organ samples were sectioned using a Leica CM1860
576 cryostat. Brain sections (30 µm thick) were collected in an anti-freeze solution containing 30%
577 sucrose (Merck Life Science, #1076515000) and 30% glycerol (VWR, #443320113) in 0.1 M
578 PBS, pH 7.4. Liver, duodenum, and pancreas sections (15 µm thick) were mounted on glass
579 slides.

580 *Immunohistochemistry*

581 Frozen sections (n = 4 per group) were washed in 0.2% Triton X-100 in PBS (PBS-T),
582 incubated in 0.3% hydrogen peroxide (H_2O_2) for 10 min, blocked with 5% normal goat serum
583 in PBS-T, and then incubated overnight at 4 °C with anti-TCF7L2 antibody (Cell Signaling

584 Technology, #2569, 1:1000) in 1% NGS. Next, sections were incubated for 1 h with
585 biotinylated goat anti-rabbit antibody (Vector Laboratories, #BA-1000, 1:500) in 1% NGS, and
586 then for 1 h in Vectastain ABC reagent (Vector Laboratories, #PK-6100). Staining was
587 developed using 0.05% DAB (Sigma-Aldrich, #D12384) and 0.01% H_2O_2. Finally, sections were
588 mounted onto SuperFrost Plus slides, dehydrated in an ethanol series (50%, 70%, 95%, and
589 99.8%), washed in xylene, and mounted using EuKitt.

590 *Immunofluorescence*

591 Frozen sections (n = 4 per group) were washed in PBS-T and blocked with 5% normal
592 donkey serum (NDS) for 1 h, and then incubated with anti-TCF7L2 antibody (1:500; 2569, Cell
593 Signaling Technology) in 1% NDS overnight at 4 °C. Sections were then incubated for 1 h with
594 a secondary antibody conjugated with Alexa Fluor 488 (donkey anti-rabbit immunoglobulin G
595 [IgG] with Alexa Fluor 488, Invitrogen, #A-21206). Slides were additionally stained with
596 Hoechst 33342 (1:10,000; #62249, Thermo Fisher Scientific), washed, and mounted with
597 Vectashield Antifade Mounting Medium (H1000, Vector Laboratories). Images were captured
598 with an Axio Imager Z2 LSM 700 Zeiss confocal microscope.

599 *Diet intervention*

600 Adult young mice (postnatal day 40-50) were fed a standard chow diet (Ssniff® -
601 E1500-04; energy: 11% fat, 23% proteins, 66% carbohydrates), high-fat diet (Ssniff® - E15742-
602 34; energy: 60% fat, 20% proteins, 20% carbohydrates) or ketogenic diet (Ssniff® E15149-30;
603 energy: 94.3% fat, 4.5% proteins and 1.2% carbohydrates) for 6 weeks.

604 *General metabolic assessment: body weight, glucose, and insulin blood level, intraperitoneal*
605 *glucose tolerance test*

606 Mice weight was measured at the beginning and end of the diet intervention (n = 6
607 per group). Plasma was collected for insulin and glucose measurements. Plasma insulin (n =
608 10 controls and 15 *Tcf7l2*-cKO mice per group) was measured using the insulin ELISA kit
609 (Merck, Sigma-Aldrich #EZRMI-13K), and glucose (n = 8 controls and 9 *Tcf7l2*-cKO mice per
610 group) using the glucose oxidase method (BioSystems, #21503) in animals fasted overnight.
611 Glucose tolerance (n= 6 per group) was assessed by intraperitoneal glucose injections (2g/kg
612 body weight) to animals fasted overnight. Blood samples were collected from the tail at 0, 15,
613 30, 60, 90, and 120 min after glucose injection.

614 *Basic locomotor activity*

615 Locomotor activity was assessed in a dimly lit three-chamber apparatus enriched with
616 objects during a 10-min session (n = 9 per group). Movement parameters were automatically
617 quantified using AnyMaze behavioral tracking software (Stoelting, Wood Dale, IL).

618 *Light-dark box*

619 A light/dark transition test (n = 9 per group) was conducted using a cage divided into
620 two equal compartments, with a small opening allowing free movement between them (Ugo
621 Basile, Italy). The open (light) compartment faced the wall to prevent the animals from seeing
622 the experimenter. Illumination in the open compartment was set to 200-400 lux, while the
623 dark compartment was maintained at ≤5 lux. Each animal was placed in the center of the light
624 compartment and allowed to explore the cage freely for 10 min. After each trial, urine and
625 fecal boli were removed, and the cage was cleaned with 70% ethanol to eliminate potential
626 olfactory cues. Recordings were analyzed to extract latency to enter the dark compartment,
627 time spent in the light and dark compartment, and the number of transitions between them.

628 *Open-field test*

An open-field test (n = 10 females per group and 8 males per group) was performed in a dark room using a black-painted square arena (90 x 90 cm), enclosed by walls (30 cm high). The center was illuminated with a 50 W halogen bulb suspended centrally 30 cm above the arena. The animal was placed in the thigmotaxic zone, facing one of the corners, and its movement was tracked for 10 min. The recordings were then analyzed to extract data on time, distance moved, and movement duration in the illuminated central zone (a circle directly corresponding to the brightly lit part of the arena) and the thigmotaxic zone (perimeter).

Buried food test

The buried food (n = 8 per group) test was used to test the olfactory function in mice. Before the test, a piece of Kellogg's Fruit Loops was added to the subjects' cages for three days. All chow pellets were removed 18-24 hours before the test. The test was conducted in a standard mouse cage with a 3 cm layer of fresh bedding. On the test day, each mouse was acclimated to the test cage for 5 min, then transferred to an empty, clean cage. The food stimulus was buried approximately 1 cm beneath the surface of the bedding in a random corner of the test cage. The mouse was then returned to the test cage, and the latency to locate the buried food was recorded.

Three-chamber test

The three-chamber social preference test (n = 9 per group) was conducted according to previous recommendations [101]. The test consisted of three distinct phases of 10 min each. The first was the habituation phase, during which the test mouse could explore the apparatus containing two empty cups. The second stage was the pre-test, where two identical objects were placed under the cups to familiarize the animal with the objects and to observe any

652 possible preference for a specific chamber. Finally, the social preference phase allowed the
653 test mouse to interact with a social stimuli - an age-, sex-, and strain-matched unfamiliar WT
654 mouse under one cup - and a non-social stimulus - a new object under the other cup. The test
655 mouse was recorded for 10 min, and the time spent interacting with the social and the non-
656 social stimulus was quantified. The area directly surrounding each cup was designated as a
657 zone of interest, and the mice's presence in this area was automatically scored for social
658 preference using the Anymaze behavior tracking software (Stoelting, Wood Dale, IL). All
659 videos were manually reviewed to verify that the animal was tracked well, and the time when
660 the animal was near the cup without any interaction with the mouse or the object was
661 removed from the final analysis. Social preference was quantified as the discrimination index:
662 (Time exploring the mouse - Time exploring the object) / (Total time spent exploring).

663 *Electronic tagging and pre-experimental housing for IntelliCage and EcoHAB*

664 Female mice were electronically tagged under brief isoflurane anesthesia by
665 subcutaneous injection of glass-covered microtransponders (11.5 mm length, 2.2 mm
666 diameter, DATAMARS for *IntelliCage*, or 9.5 mm length, 2.2 mm diameter, RFIP Ltd for
667 *EcoHAB*) for individual identification and tracking. The microtransponders emit a unique
668 animal identification code when activated by the magnetic field of RFID antennas or a
669 portable chip reader. After tagging, mice were transferred to the experimental rooms and
670 housed together for at least one week prior to placement in the *IntelliCage* or *EcoHAB*
671 systems, in order to minimize the effects of an unstable social structure and to acclimate to
672 the shifted light/dark cycle. The temperature in the experimental rooms was maintained at
673 23–24 °C, with relative humidity levels between 35% and 45%.

674 *IntelliCage*

675 The automated *IntelliCage* system consisted of a home cage equipped with four
676 conditioning chambers (corners), each fitted with two water bottles, sensors, and motorized
677 door. The cognitive assessment in this setup involved two independent cohorts per genotype,
678 n = 23 for control and n = 18 for *Tcf7l2*-cKO female mice. The experiment began with a three-
679 day simple adaptation phase (SA), followed by a two-day nose-poke adaptation phase (NP), a
680 three-day place learning phase (PL), and a reward-based discrimination learning phase (DISC).
681 During SA, doors in all conditioning units (corners) were open, and access to the two bottles
682 in each corner, filled with tap water, was unrestricted. During NP, the doors were closed by
683 default, and the mice were required to use a nose-poke response—by inserting their snouts
684 into any of the two holes on the operant corner walls to gain access to water. The door
685 remained open as long as the animal kept its snout in the hole, regardless of drinking
686 behavior. In PL, each mouse was randomly assigned to a conditioning unit that provided
687 access to water. Only one unit was available per mouse, and no more than three mice were
688 assigned to the same unit. In DISC, one bottle in each corner was filled with 10% sucrose. Mice
689 could choose between nose-poking one of two separate doors—one leading to a bottle of tap
690 water and the other to a bottle containing a reward—placed in opposite locations within the
691 conditioning corner. All visits and nose-pokes were recorded. Nose-pokes directed to the
692 bottle with reward as the first choice upon entering the conditioning unit were considered a
693 correct responses. Animals exhibiting transponder identification failure were excluded from
694 the analysis.

695 *Eco-HAB*

696 This naturalistic automated system *EcoHAB* [67] consisted of four cages connected by
697 tunnels, arranged in a looped square layout, with food and water available in two of them.
698 The behavioral assessment in this setup involved cohorts of control and *Tcf7l2*-cKO female

699 mice (three independent cohorts fed the chow diet, n = 35 for control and n = 32 for *Tcf7l2*-
700 cKO mice; two independent cohorts fed the ketogenic diet, n = 21 for control and n = 20 for
701 *Tcf7l2*-cKO mice). All mice in a tested cohort had unrestricted access to all compartments
702 throughout the 3-day experimental period. Individual mouse movements between cages
703 were tracked using RFID antennas installed on the connecting tunnels. Daily movement data
704 were processed using the custom 'DeepEcoHab' software package (see Code and data
705 availability section) to extract relevant behavioral features. Exploratory behavior was
706 quantified as the total number of visits each mouse made to all EcoHAB cages. Dynamic social
707 interactions were assessed by measuring chasing behavior between pairs of mice. In-pair
708 chasing was defined as an event where one mouse entered a tunnel, followed immediately
709 by a second mouse entering the same tunnel and both traveling together in the same
710 direction until exiting into the next cage. Passive social interactions were assessed as time
711 spent together, defined as the total duration during which both mice occupied the same cage,
712 calculated for each pair. To assess grouping behavior, this total time was then expressed as
713 the percentage of time the pair spent together in each individual cage. Animals exhibiting
714 transponder identification failure during the experiment were excluded from the analysis.

715 *Social investigative interactions between unfamiliar mice*

716 The spontaneous social interaction test was conducted in males. Four age- and strain-
717 matched unfamiliar mice were placed together into a test cage (*n* = 16 per group in 4
718 independent cohorts), and their behavior was recorded continuously for 2 hours. Nose-to-
719 nose contact and anogenital sniffing [102] were scored and quantified from the recordings.

720 *Metabolic substances extraction and 1D NMR measurements*

721 Soluble metabolites were extracted from the thalamus and cortex (n = 6 per group)
722 and separated using Bligh and Dyer method [103]. Samples were homogenized on ice with 1 ml
723 chloroform:methanol (2:1, v/v) containing 0.01% butylated hydroxytoluene as an antioxidant.
724 After adding 0.5 ml water and mixing, samples were centrifuged (3000 rpm, 10 min, 4 °C) to
725 separate phases. The aqueous phase was frozen in liquid nitrogen and freeze-dried, then
726 dissolved in deuterium oxide with 0.05% 2,2-dimethyl-2-silapentane-5-sulfonate (DSS) as an
727 internal standard and transferred into 3 mm NMR tubes. All one-dimensional ^{1}H-NMR
728 measurements were performed on the 700 MHz Agilent DirectDrive2 spectrometer equipped
729 with a room-temperature HCN probe, temperature-controlled at 25 °C. ^{1}H-NMR spectra were
730 recorded with 32K data points, acquisition time 3s, interscan delay 90s and 1250 scans. The
731 obtained 1D data sets were processed and analyzed using Mnova 12.0 software with zero-
732 filling to 128K and exponential weighting function (line broadening of 0.2 Hz). Zero-order
733 phase correction and baseline correction using the polynomial fit were done automatically on
734 each spectrum. The chemical shift scale was referenced to the 4,4-dimethyl-4-silapentane-1-
735 sulfonic acid (DSS) peak (δ = 0.00 ppm). Spectra were used for metabolite identification.
736 Lactate (Lac), alanine (Ala), glycine (Gly), asparagine (Asp), succinate (Suc), γ-aminobutyric
737 acid (GABA), taurine (Tau), N-acetylaspartic acid (NAA), creatine (Cr), myo-inositol (M-In) and
738 malic acid (MA) were identified [104,105]. Absolute integrals of representative peaks were
739 determined.

740 *High-resolution respirometry*

741 Oxygraph-2k high-resolution respirometer (Oroboros Instruments, Innsbruck, Austria)
742 was used to measure mitochondrial oxidation by substrate-driven respiration protocol [106] in
743 samples from the thalamus, cortex, and cerebellum (n = 3 per group). Tissues were

744 permeabilized with 0.005% digitonin for 30 minutes before the start of the respirometry assy.
745 Substrates were added sequentially in the following order: malate (0.5 mM),
746 palmitoylcarnitine (0.5 µM), ADP+Mg^{+2} (2 mM), octanoylcarnitine (0.2 mM), 3-
747 hydroxybutyrate (1 mM), pyruvate (5 mM), glutamate (10 mM), and succinate (10mM). The
748 integrity of the outer mitochondrial membrane was verified by the addition of cytochrome c
749 (10 µM) after the addition of all substrates. Maximum respiration was assessed through
750 stepwise addition of carbonyl cyanide m-chlorophenyl hydrazone (CCCP 0.05 µM). Complex I
751 was blocked by rotenone (0.5 µM). Complex II was inhibited by malonate (5 mM). Complex III
752 was inhibited by Antimycin A (2.5 µM). Complex IV was inhibited by sodium azide (100 mM).
753 MIR-06 buffer was used to access respiration (ethylene glycol-bis(β-aminoethyl ether)-
754 N,N,N',N'tetraacetic acid [EGTA] 0.5 mM, MgCl2 3 mM, lactobionic acid 60 mM, taurine 20
755 mM, KH2PO4 10 mM, HEPES 20 mM, d-sucrose 110 mM, both 1 mg/ml BSA–fatty acid free
756 and Catalase 280 U/mL were added freshly, pH 7.1). Palmitoylcarnitine was prepared in the
757 presence of BSA, and preliminary experiments were conducted to ensure the applied
758 concentration did not inhibit respiration. Due to limited sample availability, all substrates
759 were added within a single experimental run. Data was recorded and analyzed with DatLab
760 software (v5.1.0.20; Oroboros Instruments, Innsbruck, Austria).

761 *Statistical analysis*

762 All experiments were randomized and analyzed in a blinded manner. The required
763 sample sizes were estimated based on our previous experience with similar experiments and
764 articles published in the same research field. The indicated *n* for each experiment represents
765 the number of biological replicates. Data were tested for normality (Shapiro-Wilk) and further
766 analyzed using GraphPad Prism 9.5.1. Statistical tests were chosen based on the experimental

design and data distribution. Two-tailed Mann-Whitney test was used to compare two independent groups when data did not meet the assumptions of parametric tests. Two-tailed T-test was used to compare the means of two independent groups when data were normally distributed and variances were equal. One-way analysis of variance (ANOVA) was used to compare the means of three or more independent groups. Two-way ANOVA was used to analyze the effects of two independent variables on a dependent variable. Repeated measures ANOVA was used for time-series data. Correlations between parameters were assessed using Pearson's correlation coefficient. Differences in variance between groups were evaluated with Levene's test. In all cases, statistical significance was considered when $p < 0.05$.

Code and data availability

The algorithms and scripts comprising the 'DeepEcoHAB' package - the software implementation used to generate and analyze *EcoHAB* results reported herein - are currently under final development and are not yet publicly accessible. The package will be released under an Open Source Initiative-approved open-source license, permitting free academic use via GitHub (URL to be provided) in the last quarter of 2025. Until that release, the code is available from the coauthors of the study: Marcin Lipiec (m.lipiec@nencki.edu.pl) & Konrad Danielewski (k.danielewski@nencki.edu.pl), upon reasonable request. Raw data from *EcoHAB* test will be made available in the open-access data repository of the University of Warsaw.

Acknowledgements

This work was supported by Narodowe Centrum Nauki (NCN, National Science Center) grants 2020/37/B/NZ4/03261 and 2024/55/B/NZ4/03078 to MBW and

789 2015/19/B/NZ4/03571 to AN. Additionally, ACh and BHMM were supported by NCN grant
790 2019/35/B/NZ3/04066 awarded to ACh.

791 ## Conflict of Interest

792 AN is now an employee of AstraZeneca. Other authors declare no conflicts of interest
793 related to the work described, including conflicting financial interests.

794 ## References

795 1 Dhanasekara CS, Ancona D, Cortes L, Hu A, Rimu AH, Robohm-Leavitt C *et al.*
796 Association Between Autism Spectrum Disorders and Cardiometabolic Diseases: A
797 Systematic Review and Meta-analysis. *JAMA Pediatr* 2023; 177: 248–257.
798 2 Mitchell AJ, Vancampfort D, Sweers K, Van Winkel R, Yu W, De Hert M. Prevalence of
799 metabolic syndrome and metabolic abnormalities in schizophrenia and related
800 disorders-a systematic review and meta-analysis. Schizophr Bull. 2013; 39: 306–318.
801 3 Nagalski A, Kozinski K, Wisniewska MB. Metabolic pathways in the periphery and
802 brain: Contribution to mental disorders? *International Journal of Biochemistry and*
803 *Cell Biology* 2016; 80. doi:10.1016/j.biocel.2016.09.012.
804 4 Vancampfort D, Stubbs B, Mitchell AJ, De Hert M, Wampers M, Ward PB *et al.* Risk of
805 metabolic syndrome and its components in people with schizophrenia and related
806 psychotic disorders, bipolar disorder and major depressive disorder: a systematic
807 review and meta-analysis. *World Psychiatry* 2015; 14: 339–347.
808 5 Gao X, Qin Y, Jiao S, Hao J, Zhao J, Wang J *et al.* Genetic evidence for the causal
809 relations between metabolic syndrome and psychiatric disorders: a Mendelian
810 randomization study. *Transl Psychiatry* 2024; 14. doi:10.1038/S41398-024-02759-5.

811 6 Postolache TT, del Bosque-Plata L, Jabbour S, Vergare M, Wu R, Gragnoli C. Co-shared
812 genetics and possible risk gene pathway partially explain the comorbidity of
813 schizophrenia, major depressive disorder, type 2 diabetes, and metabolic syndrome.
814 *Am J Med Genet B Neuropsychiatr Genet* 2019; 180: 186–203.
815 7 Meijsen J, Hu K, Krebs MD, Athanasiadis G, Washbrook S, Zetterberg R *et al.*
816 Quantifying the relative importance of genetics and environment on the comorbidity
817 between mental and cardiometabolic disorders using 17 million Scandinavians. *Nat*
818 *Commun* 2024; 15. doi:10.1038/S41467-024-49507-3.
819 8 Hackinger S, Prins B, Mamakou V, Zengini E, Marouli E, Brčić L *et al.* Evidence for
820 genetic contribution to the increased risk of type 2 diabetes in schizophrenia. *Transl*
821 *Psychiatry* 2018; 8. doi:10.1038/S41398-018-0304-6.
822 9 Liu J, Xiao Q, Xiao J, Niu C, Li Y, Zhang X *et al.* Wnt/β-catenin signalling: function,
823 biological mechanisms, and therapeutic opportunities. *Signal Transduct Target Ther*
824 2022; 7. doi:10.1038/S41392-021-00762-6.
825 10 Bem J, Brożko N, Chakraborty C, Lipiec MA, Koziński K, Nagalski A *et al.* Wnt/β-catenin
826 signaling in brain development and mental disorders: keeping TCF7L2 in mind. *FEBS*
827 *Lett* 2019; 593. doi:10.1002/1873-3468.13502.
828 11 Zhang Z, Xu L, Xu X. The role of transcription factor 7-like 2 in metabolic disorders.
829 *Obesity Reviews* 2021; 22. doi:10.1111/obr.13166.
830 12 Grant SFA, Thorleifsson G, Reynisdottir I, Benediktsson R, Manolescu A, Sainz J *et al.*
831 Variant of transcription factor 7-like 2 (TCF7L2) gene confers risk of type 2 diabetes.
832 *Nat Genet* 2006; 38: 320–323.
833 13 Del Bosque-Plata L, Martínez-Martínez E, Espinoza-Camacho MÁ, Gragnoli C. The Role
834 of TCF7L2 in Type 2 Diabetes. *Diabetes* 2021; 70: 1220–1228.

835 14 Sladek R, Rocheleau G, Rung J, Dina C, Shen L, Serre D *et al.* A genome-wide
836 association study identifies novel risk loci for type 2 diabetes. *Nature* 2007; 445: 881–
837 885.
838 15 Migliorini A, Lickert H. Beyond association: A functional role for Tcf7l2 in β-cell
839 development. *Mol Metab* 2015; 4: 365–366.
840 16 Jin T. Current Understanding on Role of the Wnt Signaling Pathway Effector TCF7L2 in
841 Glucose Homeostasis. *Endocr Rev* 2016; 37: 254–277.
842 17 Shu L, Sauter NS, Schulthess FT, Matveyenko A V., Oberholzer J, Maedler K.
843 Transcription factor 7-like 2 regulates beta-cell survival and function in human
844 pancreatic islets. *Diabetes* 2008; 57: 645–653.
845 18 Da Silva Xavier G, Loder MK, McDonald A, Tarasov AI, Carzaniga R, Kronenberger K *et*
846 *al.* TCF7L2 regulates late events in insulin secretion from pancreatic islet beta-cells.
847 *Diabetes* 2009; 58: 894–905.
848 19 Boj SF, Van Es JH, Huch M, Li VSW, José A, Hatzis P *et al.* Diabetes risk gene and Wnt
849 effector Tcf7l2/TCF4 controls hepatic response to perinatal and adult metabolic
850 demand. *Cell* 2012; 151: 1595–1607.
851 20 Lee DS, An TH, Kim H, Jung E, Kim G, Oh SY *et al.* Tcf7l2 in hepatocytes regulates de
852 novo lipogenesis in diet-induced non-alcoholic fatty liver disease in mice.
853 *Diabetologia* 2023; 66: 931–954.
854 21 Geoghegan G, Simcox J, Seldin MM, Parnell TJ, Stubben C, Just S *et al.* Targeted
855 deletion of Tcf7l2 in adipocytes promotes adipocyte hypertrophy and impaired
856 glucose metabolism. *Mol Metab* 2019; 24: 44–63.

857 22 Chen X, Ayala I, Shannon C, Fourcaudot M, Acharya NK, Jenkinson CP *et al.* The
858 diabetes gene and wnt pathway effector TCF7L2 regulates adipocyte development
859 and function. *Diabetes* 2018; 67: 554–568.
860 23 Satterstrom FK, Kosmicki JA, Wang J, Breen MS, De Rubeis S, An JY *et al.* Large-Scale
861 Exome Sequencing Study Implicates Both Developmental and Functional Changes in
862 the Neurobiology of Autism. *Cell* 2020; 180: 568-584.e23.
863 24 Szewczyk LM, Lipiec MA, Liszewska E, Meyza K, Urban-Ciecko J, Kondrakiewicz L *et al.*
864 Astrocytic β-catenin signaling via TCF7L2 regulates synapse development and social
865 behavior. *Mol Psychiatry* 2024; 29: 57–73.
866 25 Stessman HAF, Xiong B, Coe BP, Wang T, Hoekzema K, Fenckova M *et al.* Targeted
867 sequencing identifies 91 neurodevelopmental-disorder risk genes with autism and
868 developmental-disability biases. *Nat Genet* 2017; 49: 515–526.
869 26 Iossifov I, O'Roak BJ, Sanders SJ, Ronemus M, Krumm N, Levy D *et al.* The contribution
870 of de novo coding mutations to autism spectrum disorder. *Nature* 2014; 515: 216–
871 221.
872 27 Dias C, Pfundt R, Kleefstra T, Shuurs-Hoeijmakers J, Boon EMJ, van Hagen JM *et al.* De
873 novo variants in TCF7L2 are associated with a syndromic neurodevelopmental
874 disorder. *Am J Med Genet A* 2021; 185: 2384–2390.
875 28 Nagalski A, Puelles L, Dabrowski M, Wegierski T, Kuznicki J, Wisniewska MB.
876 Molecular anatomy of the thalamic complex and the underlying transcription factors.
877 *Brain Struct Funct* 2016; 221: 2493–2510.
878 29 Nagalski A, Irimia M, Szewczyk L, Ferran JL, Misztal K, Kuznicki J *et al.* Postnatal
879 isoform switch and protein localization of LEF1 and TCF7L2 transcription factors in

880 cortical, thalamic, and mesencephalic regions of the adult mouse brain. *Brain Struct*
881 *Funct* 2013; 218: 1531–1549.
882 30 Lee M, Yoon J, Song H, Lee B, Lam DT, Yoon J *et al.* Tcf7l2 plays crucial roles in
883 forebrain development through regulation of thalamic and habenular neuron identity
884 and connectivity. *Dev Biol* 2017; 424: 62–76.
885 31 Lipiec MA, Bem J, Koziński K, Chakraborty C, Urban-Ciećko J, Zajkowski T *et al.* TCF7L2
886 regulates postmitotic differentiation programs and excitability patterns in the
887 thalamus. *Development* 2020. doi:10.1242/dev.190181.
888 32 Hammond E, Lang J, Maeda Y, Pleasure D, Angus-Hill M, Xu J *et al.* The Wnt effector
889 transcription factor 7-like 2 positively regulates oligodendrocyte differentiation in a
890 manner independent of Wnt/β-catenin signaling. *J Neurosci* 2015; 35: 5007–5022.
891 33 Ye F, Chen Y, Hoang T, Montgomery RL, Zhao XH, Bu H *et al.* HDAC1 and HDAC2
892 regulate oligodendrocyte differentiation by disrupting the beta-catenin-TCF
893 interaction. *Nat Neurosci* 2009; 12: 829–838.
894 34 Zhao C, Deng Y, Liu L, Yu K, Zhang L, Wang H *et al.* Dual regulatory switch through
895 interactions of Tcf7l2/Tcf4 with stage-specific partners propels oligodendroglial
896 maturation. *Nat Commun* 2016; 7. doi:10.1038/NCOMMS10883.
897 35 Duncan A, Heyer MP, Ishikawa M, Caligiuri SPB, Liu X an, Chen Z *et al.* Habenular
898 TCF7L2 links nicotine addiction to diabetes. *Nature* 2019; 574: 372–377.
899 36 Qi H, Luo L, Lu C, Chen R, Zhou X, Zhang X *et al.* TCF7L2 acts as a molecular switch in
900 midbrain to control mammal vocalization through its DNA binding domain but not
901 transcription activation domain. *Mol Psychiatry* 2023; 28: 1703–1717.
902 37 Nakajima M, Halassa MM. Thalamic control of functional cortical connectivity. *Curr*
903 *Opin Neurobiol* 2017; 44: 127–131.

904 38 Sherman SM. Thalamus plays a central role in ongoing cortical functioning. *Nat*
905 *Neurosci* 2016; 19: 533–541.
906 39 Shine JM, Lewis LD, Garrett DD, Hwang K. The impact of the human thalamus on
907 brain-wide information processing. *Nat Rev Neurosci* 2023; 24: 416–430.
908 40 Schmitt LI, Wimmer RD, Nakajima M, Happ M, Mofakham S, Halassa MM. Thalamic
909 amplification of cortical connectivity sustains attentional control. *Nature* 2017; 545:
910 219–223.
911 41 Nair A, Treiber JM, Shukla DK, Shih P, Müller R-A. Impaired thalamocortical
912 connectivity in autism spectrum disorder: a study of functional and anatomical
913 connectivity. *Brain* 2013; 136: 1942–1955.
914 42 Nair A, Carper RA, Abbott AE, Chen CP, Solders S, Nakutin S *et al.* Regional specificity
915 of aberrant thalamocortical connectivity in autism. *Hum Brain Mapp* 2015; 36: 4497–
916 4511.
917 43 Yao B, Neggers SFW, Kahn RS, Thakkar KN. Altered thalamocortical structural
918 connectivity in persons with schizophrenia and healthy siblings. *Neuroimage Clin*
919 2020; 28. doi:10.1016/J.NICL.2020.102370.
920 44 Woodward ND, Giraldo-Chica M, Rogers B, Cascio CJ. Thalamocortical dysconnectivity
921 in autism spectrum disorder: An analysis of the Autism Brain Imaging Data Exchange.
922 *Biol Psychiatry Cogn Neurosci Neuroimaging* 2017; 2: 76–84.
923 45 Anticevic A, Haut K, Murray JD, Repovs G, Yang GJ, Diehl C *et al.* Association of
924 Thalamic Dysconnectivity and Conversion to Psychosis in Youth and Young Adults at
925 Elevated Clinical Risk. *JAMA Psychiatry* 2015; 72: 882–891.

926 46 Tomasi D, Volkow ND. Reduced Local and Increased Long-Range Functional
927 Connectivity of the Thalamus in Autism Spectrum Disorder. *Cereb Cortex* 2019; 29:
928 573–585.
929 47 Park B yong, Hong SJ, Valk SL, Paquola C, Benkarim O, Bethlehem RAI *et al.*
930 Differences in subcortico-cortical interactions identified from connectome and
931 microcircuit models in autism. *Nat Commun* 2021; 12. doi:10.1038/S41467-021-
932 21732-0.
933 48 Chen P, Ye E, Jin X, Zhu Y, Wang L. Association between Thalamocortical Functional
934 Connectivity Abnormalities and Cognitive Deficits in Schizophrenia. *Sci Rep* 2019; 9.
935 doi:10.1038/S41598-019-39367-Z.
936 49 Nair A, Jalal R, Liu J, Tsang T, Mcdonald NM, Jackson L *et al.* Altered Thalamocortical
937 Connectivity in 6-Week-Old Infants at High Familial Risk for Autism Spectrum
938 Disorder. *Cerebral Cortex* 2021; 31: 4191–4205.
939 50 Brumback AC, Ellwood IT, Kjaerby C, Iafrati J, Robinson S, Lee AT *et al.* Identifying
940 specific prefrontal neurons that contribute to autism-associated abnormalities in
941 physiology and social behavior. *Mol Psychiatry* 2018; 23: 2078–2089.
942 51 Harlow EG, Till SM, Russell TA, Wijetunge LS, Kind P, Contractor A. Critical Period
943 Plasticity Is Disrupted in the Barrel Cortex of Fmr1 Knockout Mice. *Neuron* 2010; 65:
944 385–398.
945 52 Zhou T, Zhu H, Fan Z, Wang F, Chen Y, Liang H *et al.* History of winning remodels
946 thalamo-PFC circuit to reinforce social dominance. *Science* 2017; 357:162–168.
947 doi:10.1126/science.aak9726.

948 53 Nelson AC, Kapoor V, Vaughn E, Gnanasegaram JA, Rubinstein ND, Talay M *et al.*
949 Molecular and neural control of social hierarchy by a forebrain-thalamocortical
950 circuit. *Cell* 2025; 188: 5535-5554.e23.
951 54 Arakawa H, Tokashiki M, Correspondence H, Arakawa EF. The posterior intralaminar
952 thalamic nucleus promotes nose-to-nose contacts leading to prosocial reception in
953 the sequence of mouse social interaction. *European Journal of Neuroscience* 2024; 60:
954 5731–5749.
955 55 Leithead AB, Godino A, Barbier M, Harony-Nicolas H. Social Interaction Elicits Activity
956 in Glutamatergic Neurons in the Posterior Intralaminar Complex of the Thalamus. *Biol*
957 *Psychiatry* 2024; 95: 112–122.
958 56 Ferguson BR, Gao WJ. Thalamic Control of Cognition and Social Behavior Via
959 Regulation of Gamma-Aminobutyric Acidergic Signaling and Excitation/Inhibition
960 Balance in the Medial Prefrontal Cortex. *Biol Psychiatry* 2018; 83: 657–669.
961 57 Chen Z, Han Y, Ma Z, Wang X, Xu S, Tang Y *et al.* A prefrontal-thalamic circuit encodes
962 social information for social recognition. *Nat Commun* 2024; 15. doi:10.1038/s41467-
963 024-45376-y.
964 58 Keller D, Láng T, Cservenák M, Puska G, Barna J, Csillag V *et al.* A thalamo-preoptic
965 pathway promotes social grooming in rodents. *Curr Biol* 2022; 32: 4593-4606.e8.
966 59 Wells MF, Wimmer RD, Schmitt LI, Feng G, Halassa MM. Thalamic reticular
967 impairment underlies attention deficit in Ptchd1(Y/-) mice. *Nature* 2016; 532: 58–63.
968 60 Guo B, Liu T, Choi S, Mao H, Wang W, Xi K *et al.* Restoring thalamocortical circuit
969 dysfunction by correcting HCN channelopathy in Shank3 mutant mice. *Cell Rep Med*
970 2024; 5. doi:10.1016/J.XCRM.2024.101534.

61 Nakajima M, Schmitt LI, Feng G, Halassa MM. Combinatorial Targeting of Distributed Forebrain Networks Reverses Noise Hypersensitivity in a Model of Autism Spectrum Disorder. *Neuron* 2019; 104: 488-500.e11.

62 Normand EA, Crandall SR, Thorn CA, Murphy EM, Voelcker B, Browning C *et al.* Temporal and mosaic Tsc1 deletion in the developing thalamus disrupts thalamocortical circuitry, neural function, and behavior. *Neuron* 2013; 78: 895–909.

63 Jang SS, Takahashi F, Huguenard JR. Reticular thalamic hyperexcitability drives autism spectrum disorder behaviors in the Cntnap2 model of autism. *Science Advances* 2025; 11: 4682.

64 Linnemann AK, Neuman JC, Battiola TJ, Wisinski JA, Kimple ME, Davis DB. Glucagon-Like Peptide-1 Regulates Cholecystokinin Production in β-Cells to Protect From Apoptosis. *Mol Endocrinol* 2015; 29: 978–987.

65 de Souza AH, Tang J, Yadev AK, Saghafi ST, Kibbe CR, Linnemann AK *et al.* Intra-islet GLP-1, but not CCK, is necessary for β-cell function in mouse and human islets. *Sci Rep* 2020; 10. doi:10.1038/S41598-020-59799-2.

66 Egerod KL, Engelstoft MS, Grunddal K V., Nøhr MK, Secher A, Sakata I *et al.* A major lineage of enteroendocrine cells coexpress CCK, secretin, GIP, GLP-1, PYY, and neurotensin but not somatostatin. *Endocrinology* 2012; 153: 5782–5795.

67 Puścian A, Łęski S, Kasprowicz G, Winiarski M, Borowska J, Nikolaev T *et al.* Eco-HAB as a fully automated and ecologically relevant assessment of social impairments in mouse models of autism. *Elife* 2016; 5. doi:10.7554/ELIFE.19532.

68 Winiarski M, Madecka A, Yadav A, Borowska J, Wołyniak MR, Jędrzejewska-Szmek J *et al.* Information sharing within a social network is key to behavioral flexibility—Lessons from mice tested under seminaturalistic conditions. *Science Advances* 2025; 11: 7255.

995 69 Zhou Y, Park SY, Su J, Bailey K, Ottosson-Laakso E, Shcherbina L *et al.* TCF7L2 is a
996 master regulator of insulin production and processing. *Hum Mol Genet* 2014; 23:
997 6419–6431.
998 70 Lein ES, Hawrylycz MJ, Ao N, Ayres M, Bensinger A, Bernard A *et al.* Genome-wide
999 atlas of gene expression in the adult mouse brain. *Nature* 2007; 445: 168–176.
1000 71 Yao Z, van Velthoven CTJ, Kunst M, Zhang M, McMillen D, Lee C *et al.* A high-
1001 resolution transcriptomic and spatial atlas of cell types in the whole mouse brain.
1002 *Nature* 2023; 624: 317–332.
1003 72 Kolczynska K, Loza-Valdes A, Hawro I, Sumara G. Diacylglycerol-evoked activation of
1004 PKC and PKD isoforms in regulation of glucose and lipid metabolism: a review. *Lipids*
1005 *in Health and Disease 2020 19:1* 2020; 19: 1–15.
1006 73 Kim Y-K, Hammerling U, Professor V, Biophys Acta Mol Cell Biol Lipids B. The
1007 mitochondrial PKCδ/retinol Signal Complex exerts real-time Control on Energy
1008 Homeostasis. HHS Public Access Author manuscript. *Biochim Biophys Acta Mol Cell*
1009 *Biol Lipids* 2020; 1865. doi:10.1016/j.bbalip.2020.158614.
1010 74 Loots DT, Adeniji AA, Van Reenen M, Ozturk M, Brombacher F, Parihar SP. The
1011 metabolomics of a protein kinase C delta (PKCδ) knock-out mouse model.
1012 *Metabolomics* 2022; 18. doi:10.1007/S11306-022-01949-W.
1013 75 Dienel GA. Brain Glucose Metabolism: Integration of Energetics with Function. *Physiol*
1014 *Rev* 2019; 99: 949–1045.
1015 76 Alam S, Westmark CJ, McCullagh EA. Diet in treatment of autism spectrum disorders.
1016 *Front Neurosci* 2023; 16. doi:10.3389/FNINS.2022.1031016.
1017 77 Karhu E, Zukerman R, Eshraghi RS, Mittal J, Deth RC, Castejon AM *et al.* Nutritional
1018 interventions for autism spectrum disorder. *Nutr Rev* 2020; 78: 515–531.

1019 78 Varesio C, Grumi S, Zanaboni MP, Mensi MM, Chiappedi M, Pasca L *et al.* Ketogenic
1020 Dietary Therapies in Patients with Autism Spectrum Disorder: Facts or Fads? A
1021 Scoping Review and a Proposal for a Shared Protocol. *Nutrients* 2021; 13: 2057.
1022 79 Ahmad Y, Seo DS, Jang Y. Metabolic Effects of Ketogenic Diets: Exploring Whole-Body
1023 Metabolism in Connection with Adipose Tissue and Other Metabolic Organs. *Int J Mol*
1024 *Sci* 2024; 25. doi:10.3390/IJMS25137076.
1025 80 Ding H, Xie M, Wang J, Ouyang M, Huang Y, Yuan F *et al.* Shared genetics of
1026 psychiatric disorders and type 2 diabetes:a large-scale genome-wide cross-trait
1027 analysis. *J Psychiatr Res* 2023; 159: 185–195.
1028 81 Yang Y, Shen M, Li L, Long Y, Wang L, Lang B *et al.* Olanzapine Promotes the
1029 Occurrence of Metabolic Disorders in Conditional TCF7L2-Knockout Mice. *Front Cell*
1030 *Dev Biol* 2022; 10. doi:10.3389/FCELL.2022.890472.
1031 82 Mitchell RK, Mondragon A, Chen L, Mcginty JA, French PM, Ferrer J *et al.* Selective
1032 disruption of Tcf7l2 in the pancreatic β cell impairs secretory function and lowers β
1033 cell mass. *Hum Mol Genet* 2015; 24: 1390–1399.
1034 83 Da Silva Xavier G, Mondragon A, Sun G, Chen L, McGinty JA, French PM *et al.*
1035 Abnormal glucose tolerance and insulin secretion in pancreas-specific Tcf7l2-null
1036 mice. *Diabetologia* 2012; 55: 2667–2676.
1037 84 Savic D, Ye H, Aneas I, Park SY, Bell GI, Nobrega MA. Alterations in TCF7L2 expression
1038 define its role as a key regulator of glucose metabolism. *Genome Res* 2011; 21: 1417–
1039 1425.
1040 85 Zhai J, Li X, Zhou Y, Fan L, Xia W, Wang X *et al.* Correlation and predictive ability of
1041 sensory characteristics and social interaction in children with autism spectrum
1042 disorder. *Front Psychiatry* 2023; 14. doi:10.3389/FPSYT.2023.1056051.

1043 86 Kojovic N, Hadid L Ben, Franchini M, Schaer M. Sensory Processing Issues and Their
1044 Association with Social Difficulties in Children with Autism Spectrum Disorders. *J Clin*
1045 *Med* 2019; 8. doi:10.3390/JCM8101508.
1046 87 Manji H, Kato T, Di Prospero NA, Ness S, Beal MF, Krams M *et al.* Impaired
1047 mitochondrial function in psychiatric disorders. *Nat Rev Neurosci* 2012; 13: 293–307.
1048 88 Rossignol DA, Frye RE. Mitochondrial dysfunction in autism spectrum disorders: a
1049 systematic review and meta-analysis. *Mol Psychiatry* 2012; 17: 290–314.
1050 89 Rowland LM, Pradhan S, Korenic S, Wijtenburg SA, Hong LE, Edden RA *et al.* Elevated
1051 brain lactate in schizophrenia: a 7 T magnetic resonance spectroscopy study. *Transl*
1052 *Psychiatry* 2016; 6. doi:10.1038/tp.2016.239.
1053 90 Frye RE, Rincon N, McCarty PJ, Brister D, Scheck AC, Rossignol DA. Biomarkers of
1054 mitochondrial dysfunction in autism spectrum disorder: A systematic review and
1055 meta-analysis. *Neurobiol Dis* 2024; 197. doi:10.1016/J.NBD.2024.106520.
1056 91 Goh S, Dong Z, Zhang Y, DiMauro S, Peterson BS. Mitochondrial dysfunction as a
1057 neurobiological subtype of autism spectrum disorder: evidence from brain imaging.
1058 *JAMA Psychiatry* 2014; 71: 665–671.
1059 92 Maier S, Nickel K, Lange T, Oeltzschner G, Dacko M, Endres D *et al.* Increased cerebral
1060 lactate levels in adults with autism spectrum disorders compared to non-autistic
1061 controls: a magnetic resonance spectroscopy study. *Mol Autism* 2023; 14.
1062 doi:10.1186/S13229-023-00577-Y.
1063 93 Lingampelly SS, Naviaux JC, Heuer LS, Monk JM, Li K, Wang L *et al.* Metabolic network
1064 analysis of pre-ASD newborns and 5-year-old children with autism spectrum disorder.
1065 *Commun Biol* 2024; 7. doi:10.1038/S42003-024-06102-Y.

1066 94 Vallée A, Vallée J-N. Warburg effect hypothesis in autism Spectrum disorders. *Mol*
1067 *Brain* 2018; 11. doi:10.1186/s13041-017-0343-6.
1068 95 Nakagami Y, Sugihara G, Nakashima N, Hazama M, Son S, Ma S *et al.* Anti-PDHA1
1069 antibody is detected in a subset of patients with schizophrenia. *Scientific Reports*
1070 *2020 10:1* 2020; 10: 1–12.
1071 96 Sofou K, Dahlin M, Hallböök T, Lindefeldt M, Viggedal G, Darin N. Ketogenic diet in
1072 pyruvate dehydrogenase complex deficiency: short- and long-term outcomes. *J*
1073 *Inherit Metab Dis* 2017; 40: 237–245.
1074 97 Li R, Ma M, Chen W, Qiu Z. Classic ketogenic diet-induced ketoacidosis in the
1075 treatment of pyruvate dehydrogenase deficiency: a case report and literature review.
1076 *BMC Pediatr* 2024; 24. doi:10.1186/S12887-024-05054-W.
1077 98 Wei SJ, Schell JR, Chocron ES, Varmazyad M, Xu G, Chen WH *et al.* Ketogenic diet
1078 induces p53-dependent cellular senescence in multiple organs. *Sci Adv* 2024; 10:
1079 1463.
1080 99 Long F, Bhatti MR, Kellenberger A, Sun W, Modica S, Höring M *et al.* A low-
1081 carbohydrate diet induces hepatic insulin resistance and metabolic associated fatty
1082 liver disease in mice. *Mol Metab* 2023; 69. doi:10.1016/j.molmet.2023.101675.
1083 100 Kossoff EH, Zupec-Kania BA, Rho JM. Ketogenic diets: an update for child neurologists.
1084 *J Child Neurol* 2009; 24: 979–988.
1085 101 Rein B, Ma K, Yan Z. A standardized social preference protocol for measuring social
1086 deficits in mouse models of autism. *Nature Protocols 2020 15:10* 2020; 15: 3464–
1087 3477.

1088 102 Weissbrod A, Shapiro A, Vasserman G, Edry L, Dayan M, Yitzhaky A *et al.* Automated
1089 long-term tracking and social behavioural phenotyping of animal colonies within a
1090 semi-natural environment. *Nat Commun* 2013; 4. doi:10.1038/ncomms3018.
1091 103 Bligh EG, Dyer WJ. A rapid method of total lipid extraction and purification. *Can J*
1092 *Biochem Physiol* 1959; 37: 911–917.
1093 104 Cruz T, Gleizes M, Balayssac S, Mornet E, Marsal G, Millán JL *et al.* Identification of
1094 altered brain metabolites associated with TNAP activity in a mouse model of
1095 hypophosphatasia using untargeted NMR-based metabolomics analysis. *J Neurochem*
1096 2017; 140: 919–940.
1097 105 Graham SF, Holscher C, McClean P, Elliott CT, Green BD. 1H NMR metabolomics
1098 investigation of an Alzheimer's disease (AD) mouse model pinpoints important
1099 biochemical disturbances in brain and plasma. *Metabolomics* 2013; 9: 974–983.
1100 106 Sánchez-González C, Formentini L. An optimized protocol for coupling oxygen
1101 consumption rates with β-oxidation in isolated mitochondria from mouse soleus.
1102 *STAR Protoc* 2021; 2. doi:10.1016/J.XPRO.2021.100735.
1103

1060 **Fig. 1. Cre-mediated recombination of *Tcf7l2* in *Cck*-expressing cells depletes TCF7L2 in the**
1061 **thalamus and partially in the pancreas, inducing a concurrent prediabetic state**

1062 **(A)** DAB immunohistochemical staining of TCF7L2 in coronal brain sections from P60 control
1063 (CTR) and Cck^{Cre}:$Tcf7l2^{fl/fl}$ (cKO) male mice; white dotted lines demarcate the thalamus. **(B)**
1064 Western blot analysis of TCF7L2 in the thalamus from P60 male mice; the upper band
1065 represents the long isoform, and the lower band the short isoform of TCF7L2. **(C)**
1066 Immunofluorescent staining of TCF7L2 (green) in the pancreas of the Cck^{Cre}:$TdTomato^{fl/fl}$
1067 reporter line at P60. **(D)** Western blot analysis of TCF7L2 in the pancreas from P60 male mice;
1068 only the long isoform of TCF7L2 is present. **(E)** Immunofluorescent staining of TCF7L2 (green)
1069 in the liver from the Cck^{Cre}:$TdTomato^{fl/fl}$ reporter line at P14. **(F)** Western blot analysis of
1070 TCF7L2 in the liver from P60 male mice. **(G)** Schematic of the dietary intervention showing the
1071 nutrient composition of the standard laboratory (Chow) and high-fat (HF) diet; only males
1072 were tested. **(H)** Percentage increase in body mass in male mice fed the chow or HF diet. **(I)**
1073 Fasting blood insulin levels. **(J)** Fasting blood glucose levels. **(K)** Glucose tolerance test (GTT;
1074 left panel); area under the curve (AUC) of GTT for the same groups (right panel); n = 6.

1075 Bars in H, I and J represent mean values, with dots indicating individual mice; dots in K
1076 represent mean values. Data in H, I, J, and K right panel were analyzed with two-way ANOVA
1077 followed by Tukey's multiple comparison test. **$p < 0.01$, ***$p < 0.001$, ****$p < 0.0001$.

1078

1079

1080

1081

1082

1083 **Fig. 2. TCF7L2 depletion in the thalamus does not cause apparent alterations in locomotor,**

1084 **anxiety-related, or cognitive performance**

1085 **(A)** Schematic of a dimly light enclosure enriched with objects; both sexes were tested. Data

1086 were recorded for 10 minutes. **(B)** Immobility time of control (CTR) and *Cck*^{Cre}*:Tcf7l2*$^{fl/fl}$ (cKO)

1087 mice. **(C)** Average (left panel) and maximum (right panel) speed when moving. **(D)** Average

1088 angular velocity. **(E)** Schematic of the buried food test used to assess olfactory function; both

1089 sexes were tested. **(F)** Latency to retrieve hidden food. **(G)** Schematic of the open field test;

1090 both sexes were tested. **(H)** Time spent in the center or the perimeter of the open field. **(I)**

1091 Mobility speed in the center or the perimeter of the open field. **(J)** Schematic of the *Intellicage*

1092 setup used to assess learning and motivation. During the nose-poke adaptation phase (days

1093 4-5), mice accessed water in all corners and learned to nose-poke; in the place learning phase

1094 (PL, days 6-8), each mouse was assigned a specific corner, while the remaining corners were

1095 inaccessible, in the cue discrimination (reward-based learning) phase (DISC, days 9-13), one

1096 corner bottle was replaced with 10% sucrose. CTR n = 23 and cKO n = 18 in two independent

1097 cohorts for each genotype; only females were tested; results in K-L represent data from the

1098 dark phase. **(K)** Percentage of visits to the correct (assigned) corner relative to total visits to

1099 all corners, days 6–8. **(L)** Percentage of visits to the sucrose-containing bottle relative to total

1100 visits to the correct corner, days 9–12.

1101 Bars in graphs B, C, D, F, H, and I represent mean values, with dots indicating individual mice;

1102 dots in K and L represent mean values. Data in B, C, D, and F were analyzed using an unpaired

1103 T-test; data in H, I, K, and L were analyzed using two-way ANOVA followed by Tukey's multiple

1104 comparison test.

1105

1106 **Fig. 3. Postnatal thalamic knockout of *Tcf7l2* leads to social deficits**

1107 **(A)** Schematic of the three-chamber social interest test; a mouse was presented with an
1108 unfamiliar mouse and an object; both sexes were tested. **(B)** Preference for a mouse over an
1109 object, calculated for control (CTR) and *Cck*^{Cre}*:Tcf7l2*$^{fl/fl}$ (cKO) mice as the discrimination index.
1110 **(C)** Schematic of the *Intellicage* setup showing water access in four corners during the simple
1111 adaptation phase (days 1-3). CTR n = 23 and cKO n = 18 in two independent cohorts for each
1112 genotype; only females were tested; results in D-E represent data from the dark phase. **(D)**
1113 Number of visits to all corners. **(E)** Percentage of each mouse's visits to the group's most
1114 preferred corner (Pref.) or non-preferred corners (Non-pref.), relative to its total number of
1115 visits on each of three days; an alternative visualization of the same result is provided as a bar
1116 plot in SFig. 5B. **(F)** Schematic of the *EcoHAB* setup used to assess social behavior. The setup
1117 consisted of four cages connected by tunnels with antennas to track mouse movements. CTR
1118 n = 35 and cKO n = 32 in three independent cohorts for each genotype; only females were
1119 tested; results in G-I represent data from the dark phase. **(G)** Exploratory behavior, measured
1120 as the total number of visits to all cages. **(H)** In-pair chasing events, measured as one mouse
1121 trailing another through a tunnel for each mouse pair; an alternative visualization of the same
1122 result is provided as a bar plot in SFig. 5E. **(I)** Representative heatmaps (right panel) showing
1123 the number of in-pair chasing events for one control and one cKO cohort; columns represent
1124 chasing mice, rows represent chased mice; the scale was limited to 20 for better visualization
1125 of the result. **(J)** Percentage of in-pair time spent spent together in the group's most preferred
1126 cage (Pref.) or non-preferred cages (Non-pref.), relative to total time spent together,
1127 calculated for each pair across days 1–3. **(K)** Representative heatmaps, from the same cohort
1128 as in panel I, showing in-pair time spent together for one control and one cKO cohort; the
1129 scale was limited to 20 for better visualization of the result. **(L)** Schematic of the social

interaction test; four unfamiliar mice were placed in a cage for two hours; only males were tested. **(M)** Number of nose-to-nose (right panel) and anogenital sniffing (right panel) events. Bars in D, G, H, and M represent mean values, with dots indicating individual mice; violin plots in E, H, and J represent the distribution of individual data points, with the central line indicating the median and dashed lines indicating the interquartile range. Data in B were analyzed using an unpaired T-test; data in E and J were analyzed using two-way ANOVA followed by Tukey's multiple comparison test; data in D, G, H, and M were analyzed using repeated measures two-way ANOVA followed by Tukey's multiple comparison test. *$p < 0.05$, **$p < 0.01$, ***$p < 0.001$.

1153 **Fig. 4. Postnatal thalamic knockout of *Tcf7l2* influences metabolic gene expression and**
1154 **pyruvate dehydrogenase activity, affecting the utilization of pyruvate in the thalamus and**
1155 **cortex**

1156 **(A)** Upregulated and downregulated genes in the thalamic region of Cck^{Cre}:$Tcf7l2^{fl/fl}$ (cKO) mice
1157 compared to control (CTR) mice. Genes were manually curated into the functional categories
1158 indicated on the left. Log_2-transformed expression fold changes (cKO/CTR), centered to the
1159 median of each row, are displayed using a magenta–green color scale, each column
1160 represents an independent biological replicate. Right panel: thalamic enrichment (Th) is
1161 based on the Allen Brain Atlas; neuronal enrichment (Neu) is based on a whole-brain single-
1162 cell RNA-seq database, and positive TCF7L2 ChIP signal is based on our published results. **(B)**
1163 Schematic of a hypothetical signaling pathway affected by the conditional knockout of *Tcf7l2*.
1164 **(C)** Western blot analysis of PKCδ, PDHE1α, and phospho-PDHE1α in the thalamus of male
1165 mice. **(D)** Schematic of the dietary intervention showing the nutrient composition of the
1166 standard laboratory (Chow) and high-fat (HF) diet, followed by brain sectioning for 1D NMR
1167 analysis; only males were tested. **(E-F)** Levels of lactate and alanine in the thalamus and cortex
1168 of mice fed the Chow or HF diet. **(G)** Schematic of brain sectioning and subsequent cell
1169 permeabilization for high-resolution respirometry analysis; both sexes were tested. **(H-I)**
1170 Oxygen consumption rates (OCR) of permeabilized tissue membranes isolated from the
1171 thalamus and cortex of female and male mice. Data were obtained by sequentially adding
1172 fatty acids, 3-β-hydroxybutyrate, and pyruvate + glutamate to the Oxygraph-2k chamber.

1173 Bars in graphs represent mean values, with dots indicating individual mice. Data in C, E, F, H,
1174 and I were analyzed using an unpaired T-test. *$p < 0.05$, **$p < 0.01$, ***$p < 0.001$,
1175 ****$p < 0.0001$.

1176 **Fig. 5. Ketogenic diet ameliorates brain metabolic and social deficits induced by postnatal**
1177 **thalamic knockout of *Tcf7l2*.**

1178 **(A)** Schematic of the dietary intervention showing the nutrient composition of the ketogenic
1179 (Keto) diet. **(B)** Brain regions analyzed by high-resolution respirometry in permeabilized cells.
1180 **(C-D)** Oxygen consumption rates (OCR) of permeabilized tissue membranes isolated from the
1181 thalamus or cortex of female and male control (CTR) and Cck^{Cre}:$Tcf7l2^{fl/fl}$ (cKO) mice fed either
1182 the Chow or Keto diet. Data was obtained by sequentially adding fatty acids, 3-β-
1183 hydroxybutyrate, and pyruvate + glutamate to the Oxygraph-2k chamber. **(E)** Schematic of
1184 the three-chamber social interest test, in which a mouse is presented with an unfamiliar
1185 mouse and an object; only females were tested. **(F)** Preference for a mouse over an object,
1186 calculated as the discrimination index. **(G)** Schematic of the *EcoHAB* setup used to assess
1187 social behavior. The setup consisted of four cages connected by tunnels with antennas to
1188 track mouse movements. CTR n = 21 and cKO n = 20 in two independent cohorts for each
1189 genotype; only females were tested; results in H-J represent data from the dark phase, days
1190 1-3. **(H)** Exploratory behavior, measured as the total number of visits to all cages. **(I)** In-pair
1191 chasing events, measured as one mouse trailing another through a tunnel for each mouse
1192 pair; an alternative visualization of the same result is provided as a bar plot in SFig. 11D. **(J)**
1193 Representative heatmaps showing the number of in-pair chasing events from one CTR and
1194 one cKO cohort; columns represent chasing mice, rows represent chased mice; the scale was
1195 limited to 20 for better visualization of the results. **(K)** Percentage of in-pair time spent
1196 together in the group's most preferred cage (Pref.) or non-preferred cages (Non-pref.),
1197 relative to total time spent together, calculated for each pair across days 1–3. **(L)**
1198 Representative heatmaps, from the same cohort as in panel J, showing in-pair time spent
1199 together for one control and one cKO cohort; the scale was limited to 20 for better

1200 visualization of the result. **(M)** Schematic of the social interaction test; four unfamiliar mice
1201 were placed in a cage for two hours; only males were tested. **(N)** Number of nose-to-nose
1202 (right panel) and anogenital sniffing (right panel) events.

1203 Bars in C, D, F, H, and N represent mean values, with dots indicating individual mice; violin
1204 plots in I and K represent the distribution of individual data points, with the central line
1205 indicating the median and dashed lines indicating the interquartile range. Data in C, D, and F
1206 were analyzed using an unpaired T-test; data in H, I, and N were analyzed using repeated
1207 measures two-way ANOVA followed by Tukey's multiple comparison test; data in K were
1208 analyzed using two-way ANOVA followed by Tukey's multiple comparison test. *$p < 0.05$,
1209 **$p < 0.01$, ***$p < 0.001$, ****$p < 0.0001$.

1210

1211

1212

Figure 1

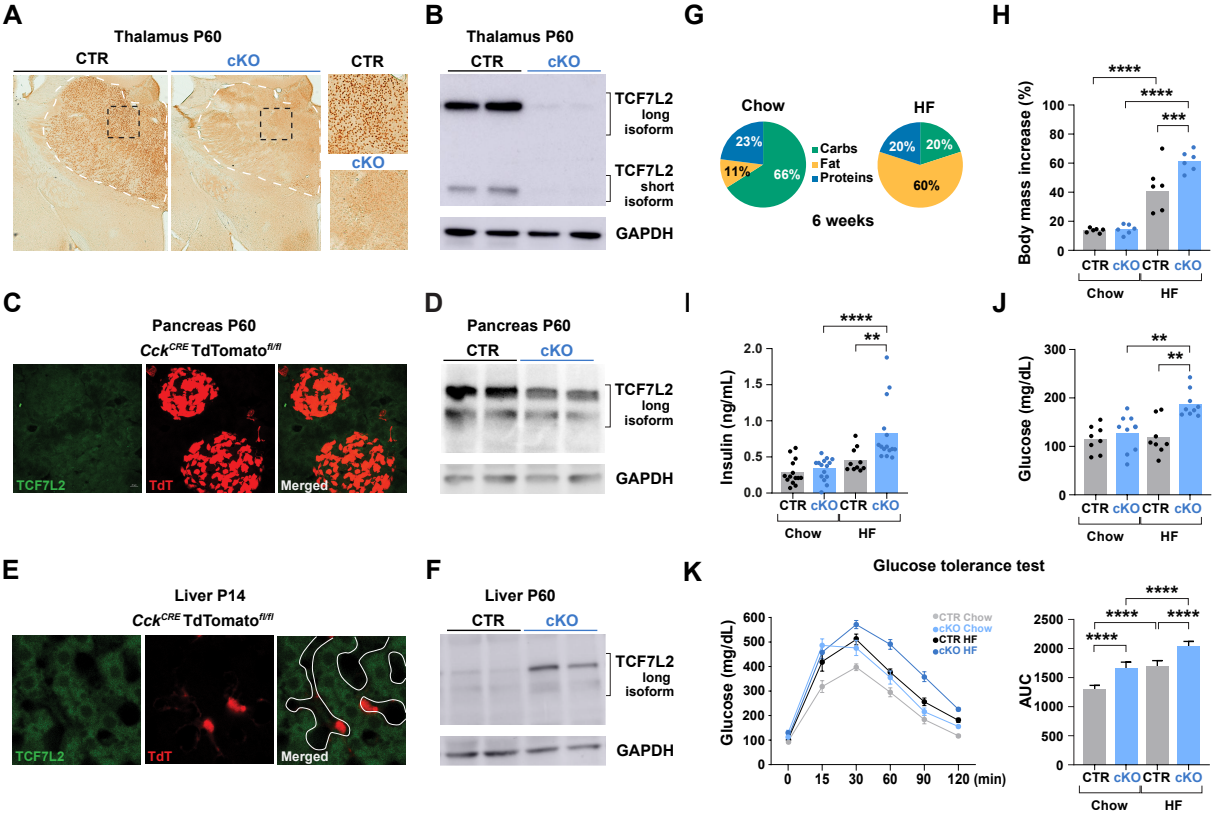
A
Thalamus P60
CTR
cKO
CTR
cKO
B
Thalamus P60
CTR
cKO
TCF7L2 long isoform
TCF7L2 short isoform
GAPDH
G
Chow
HF
23%
11%
66%
20%
20%
60%
Carbs
Fat
Proteins
6 weeks
H
Body mass increase (%)
****
****
***
CTR cKO CTR cKO
Chow HF
C
Pancreas P60
Cck^CRE TdTomato^fl/fl
TCF7L2
TdT
Merged
D
Pancreas P60
CTR
cKO
TCF7L2 long isoform
GAPDH
I
Insulin (ng/mL)
****
**
CTR cKO CTR cKO
Chow HF
J
Glucose (mg/dL)
**
**
CTR cKO CTR cKO
Chow HF
E
Liver P14
Cck^CRE TdTomato^fl/fl
TCF7L2
TdT
Merged
F
Liver P60
CTR
cKO
TCF7L2 long isoform
GAPDH
K
Glucose tolerance test
Glucose (mg/dL)
CTR Chow
cKO Chow
CTR HF
cKO HF
0 15 30 60 90 120 (min)
AUC
****
****
****
****
CTR cKO CTR cKO
Chow HF

Figure 2

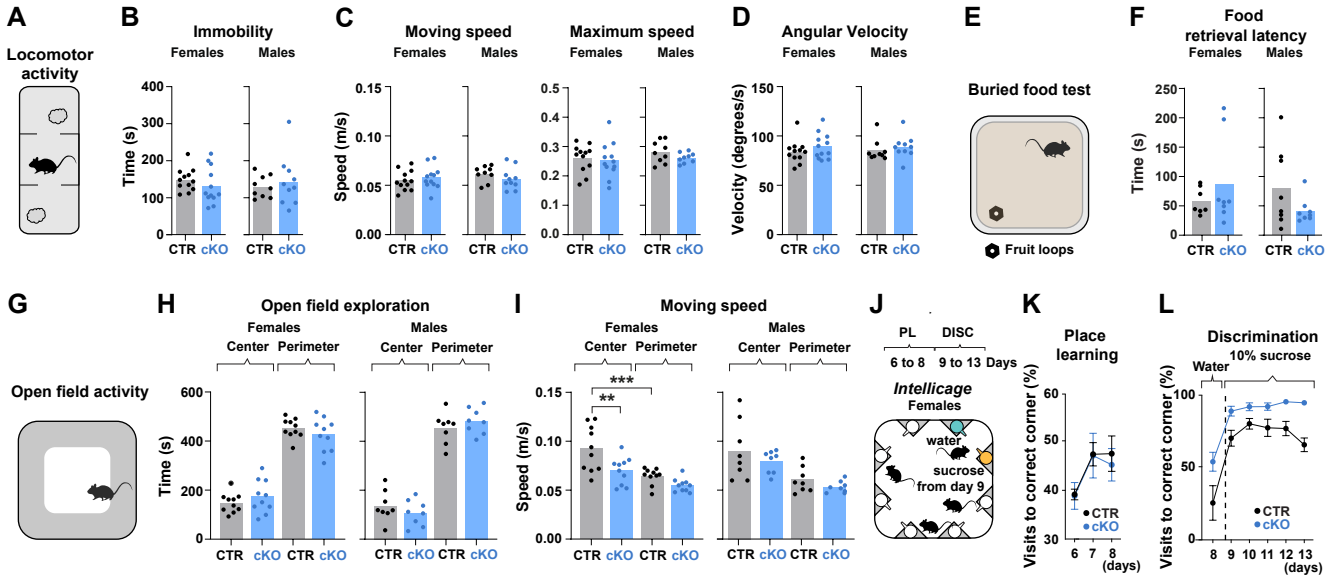
A
Locomotor activity
B
Immobility
Females
Males
Time (s)
400
300
200
100
0
CTR cKO CTR cKO
C
Moving speed
Maximum speed
Females
Males
Speed (m/s)
0.15
0.10
0.05
0.00
0.5
0.4
0.3
0.2
0.1
0.0
CTR cKO CTR cKO
D
Angular Velocity
Females
Males
Velocity (degrees/s)
150
100
50
0
CTR cKO CTR cKO
E
Buried food test
Fruit loops
F
Food retrieval latency
Females
Males
Time (s)
250
200
150
100
50
0
CTR cKO CTR cKO
G
Open field activity
H
Open field exploration
Females
Males
Center
Perimeter
Time (s)
600
400
200
0
CTR cKO CTR cKO
I
Moving speed
Females
Males
Center
Perimeter
Speed (m/s)
0.15
0.10
0.05
0.00
***
**
CTR cKO CTR cKO
J
PL
DISC
6 to 8
9 to 13 Days
Intellicage
Females
water
sucrose
from day 9
K
Place learning
Visits to correct corner (%)
60
50
40
30
CTR
cKO
6 7 8
(days)
L
Discrimination
Water
10% sucrose
Visits to correct corner (%)
100
50
0
CTR
cKO
8 9 10 11 12 13
(days)

Figure 3

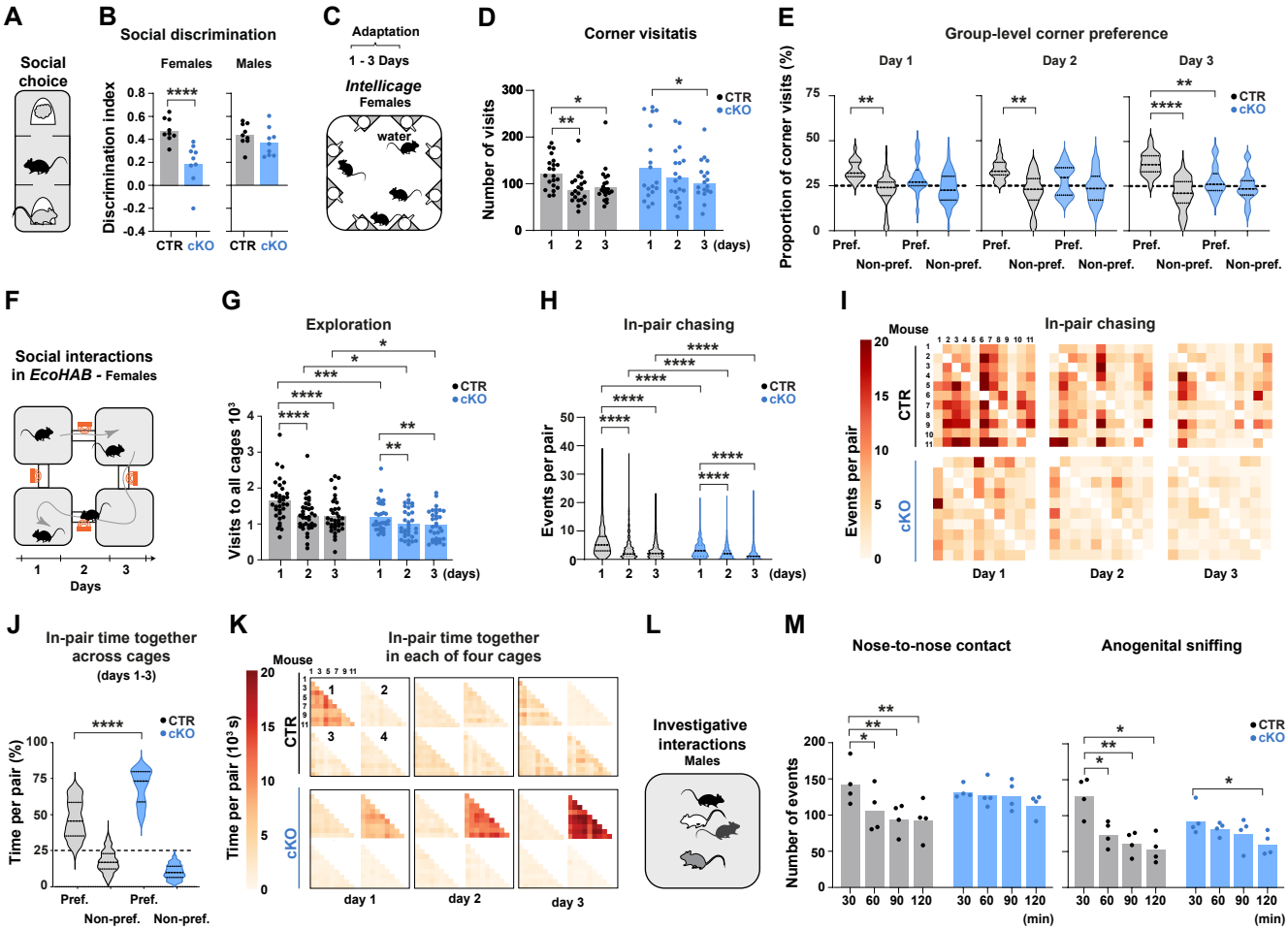
A
Social choice
B
Social discrimination
Females
Males
Discrimination index
CTR
cKO
C
Adaptation
1 - 3 Days
Intellicage
Females
water
D
Corner visitatis
Number of visits
CTR
cKO
(days)
E
Group-level corner preference
Day 1
Day 2
Day 3
Proportion of corner visits (%)
Pref.
Non-pref.
F
Social interactions in EcoHAB - Females
Days
G
Exploration
Visits to all cages 10³
(days)
H
In-pair chasing
Events per pair
(days)
I
In-pair chasing
Mouse
Events per pair
Day 1
Day 2
Day 3
J
In-pair time together across cages
(days 1-3)
Time per pair (%)
Pref.
Non-pref.
K
In-pair time together in each of four cages
Mouse
Time per pair (10³ s)
day 1
day 2
day 3
L
Investigative interactions
Males
M
Nose-to-nose contact
Anogenital sniffing
Number of events
(min)

Figure 4

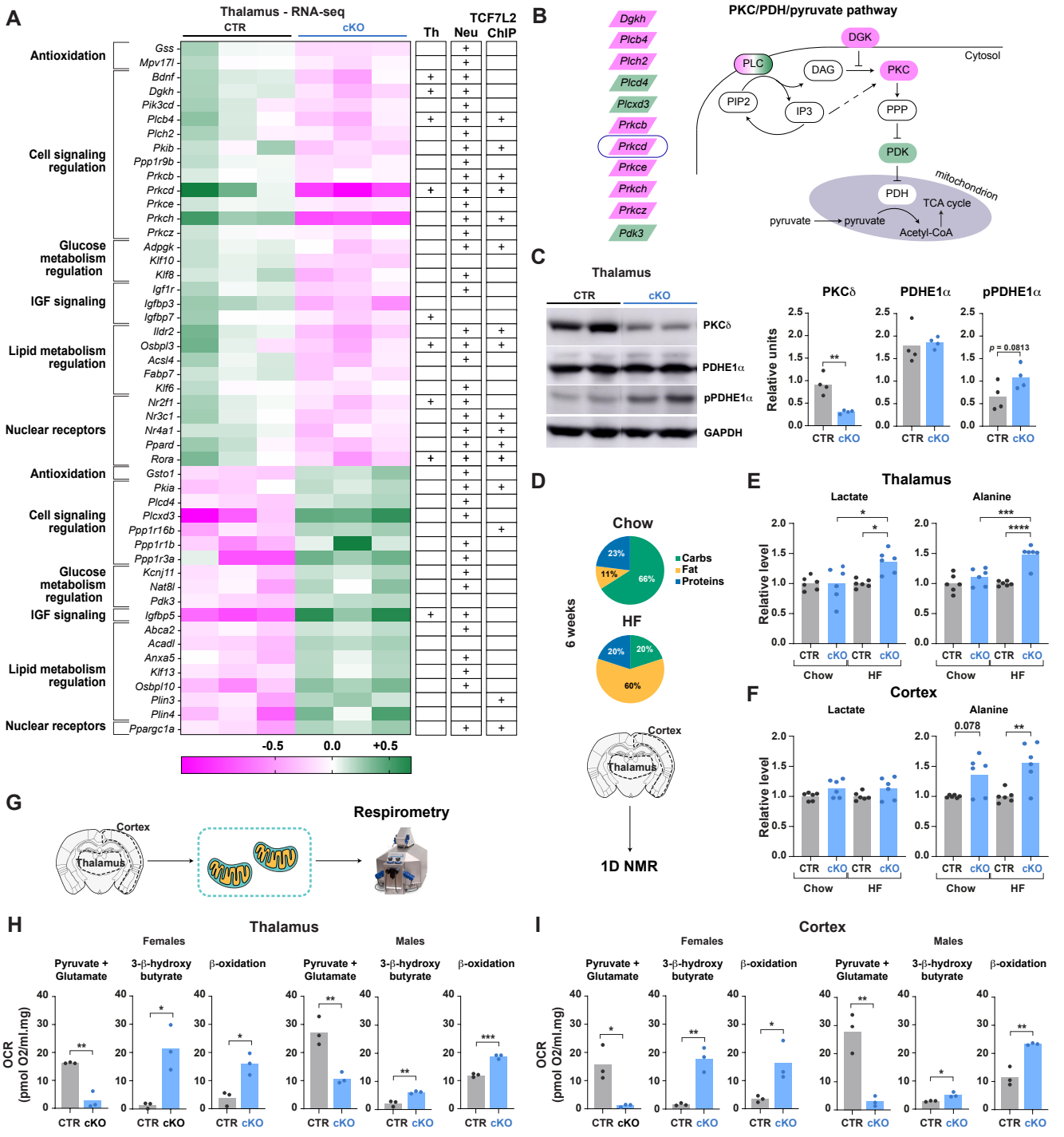
A
Thalamus - RNA-seq
CTR
cKO
Th
Neu
TCF7L2 ChIP
Antioxidation
Cell signaling regulation
Glucose metabolism regulation
IGF signaling
Lipid metabolism regulation
Nuclear receptors
Antioxidation
Cell signaling regulation
Glucose metabolism regulation
IGF signaling
Lipid metabolism regulation
Nuclear receptors
Gss
Mpv17l
Bdnf
Dgkh
Pik3cd
Plcb4
Plch2
Pkib
Ppp1r9b
Prkcb
Prkcd
Prkce
Prkch
Prkcz
Adpgk
Klf10
Klf8
Igf1r
Igfbp3
Igfbp7
Ildr2
Osbpl3
Acsl4
Fabp7
Klf6
Nr2f1
Nr3c1
Nr4a1
Ppard
Rora
Gsto1
Pkia
Plcd4
Plcxd3
Ppp1r16b
Ppp1r1b
Ppp1r3a
Kcnj11
Nat8l
Pdk3
Igfbp5
Abca2
Acadl
Anxa5
Klf13
Osbpl10
Plin3
Plin4
Ppargc1a
-0.5
0.0
+0.5
B
Dgkh
Plcb4
Plch2
Plcd4
Plcxd3
Prkcb
Prkcd
Prkce
Prkch
Prkcz
Pdk3
PKC/PDH/pyruvate pathway
DGK
Cytosol
PLC
DAG
PKC
PIP2
IP3
PPP
PDK
mitochondrion
PDH
TCA cycle
pyruvate
pyruvate
Acetyl-CoA
C
Thalamus
CTR
cKO
PKCδ
PDHE1α
pPDHE1α
GAPDH
PKCδ
PDHE1α
pPDHE1α
Relative units
P = 0.0813
D
Chow
23%
11%
66%
Carbs
Fat
Proteins
6 weeks
HF
20%
20%
60%
Cortex
Thalamus
1D NMR
E
Thalamus
Lactate
Alanine
Relative level
CTR
cKO
Chow
HF
F
Cortex
Lactate
Alanine
0.078
Relative level
G
Cortex
Thalamus
Respirometry
H
Thalamus
Females
Males
Pyruvate + Glutamate
3-β-hydroxy butyrate
β-oxidation
OCR (pmol O2/ml.mg)
CTR
cKO
I
Cortex
Females
Males
Pyruvate + Glutamate
3-β-hydroxy butyrate
β-oxidation
OCR (pmol O2/ml.mg)
CTR
cKO

Figure 5

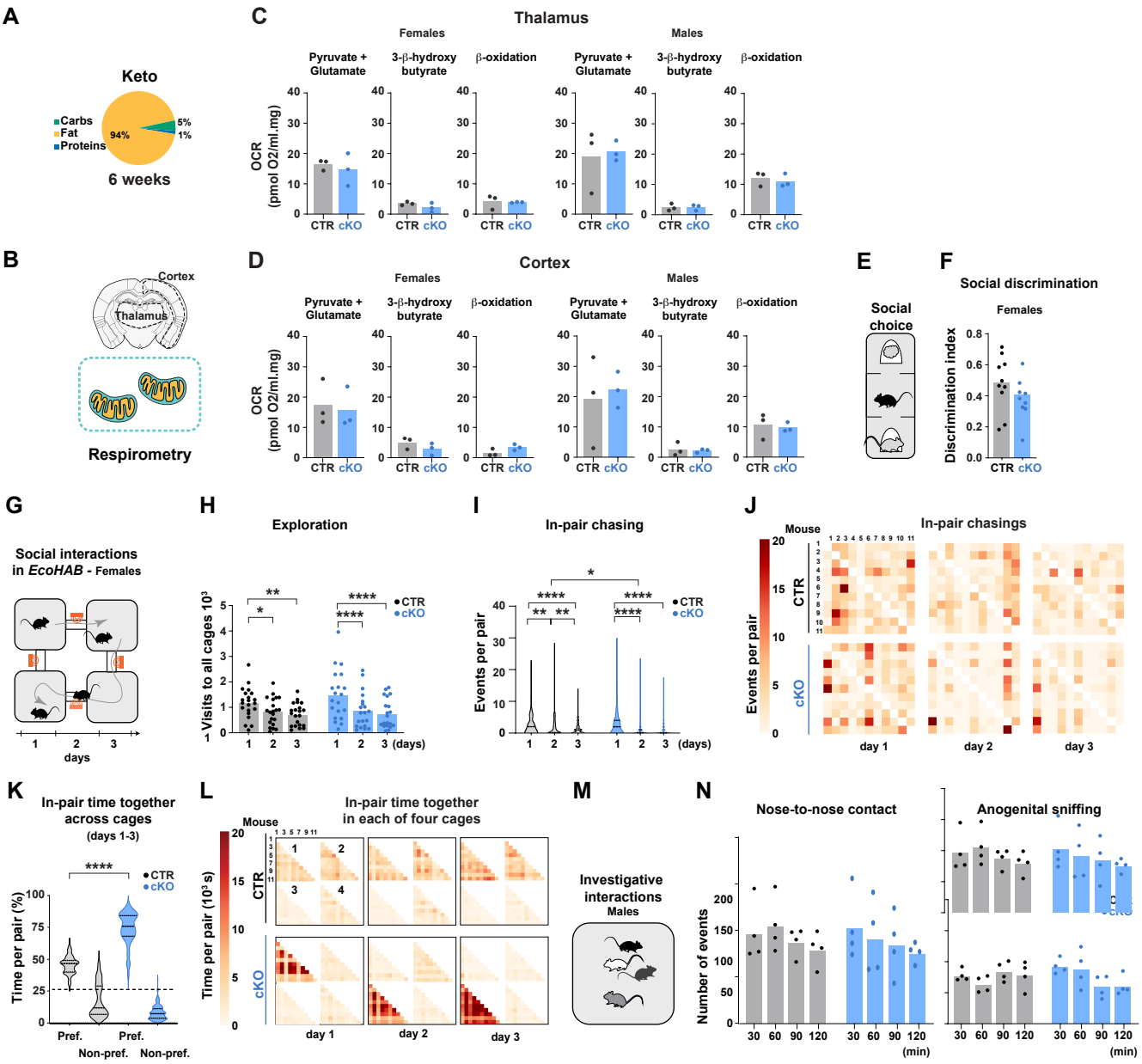
A
Keto
Carbs
Fat
Proteins
94%
5%
1%
6 weeks
B
Cortex
Thalamus
Respirometry
C
Thalamus
Females
Males
Pyruvate + Glutamate
3-β-hydroxy butyrate
β-oxidation
OCR (pmol O2/ml.mg)
CTR
cKO
D
Cortex
E
Social choice
F
Social discrimination
Females
Discrimination index
G
Social interactions in EcoHAB - Females
days
H
Exploration
Visits to all cages 10³
(days)
I
In-pair chasing
Events per pair
J
In-pair chasings
Mouse
day 1
day 2
day 3
K
In-pair time together across cages
(days 1-3)
Time per pair (%)
Pref.
Non-pref.
L
In-pair time together in each of four cages
Time per pair (10³ s)
M
Investigative interactions
Males
N
Nose-to-nose contact
Anogenital sniffing
Number of events
(min)